Dust extinction map of the Galactic plane based on the UKIDSS survey data

Downloaded from: https://research.chalmers.se, 2026-10-14 17:42 UTC

Citation for the original published paper (version of record):
Zhang, M., Kainulainen, J., Zhao, H. et al (2025). Dust extinction map of the Galactic plane based on the UKIDSS survey data. Monthly Notices of the Royal Astronomical Society, 543(4): 3830-3848. http://dx.doi.org/10.1093/mnras/staf1704

N.B. When citing this work, cite the original published paper.

research.chalmers.se offers the possibility of retrieving research publications produced at Chalmers University of Technology. It covers all kind of research output: articles, dissertations, conference papers, reports etc. since 2004. research.chalmers.se is administrated and maintained by Chalmers Library

(article starts on next page)

Monthly Notices of the ROYAL ASTRONOMICAL SOCIETY

MNRAS **543,** 3830–3848 (2025) https://doi.org/10.1093/mnras/staf1704
Advance Access publication 2025 October 7

Dust extinction map of the Galactic plane based on the UKIDSS survey data

M. Zhang [1]★ J. Kainulainen,[2] H. Zhao,[1] Y. Su,[1] M. Fang,[1] Y. Ma,[1] Z. Chen [1] and Z. Jiang[1]

[1]*Purple Mountain Observatory, and Key Laboratory for Radio Astronomy, Chinese Academy of Sciences, Nanjing 210023, China*
[2]*Department of Space, Earth and Environment, Chalmers University of Technology, SE-412 93 Gothenburg, Sweden*

Accepted 2025 September 28. Received 2025 September 28; in original form 2024 November 15

ABSTRACT

Dust plays a critical role in the study of the interstellar medium. Extinction maps derived from optical surveys often fail to capture regions with high column density due to the limited photometric depth in optical wavelengths. To address these limitations, we developed the XPNICER method based on near-infrared photometric survey data. This method combines the previously established PNICER and Xpercentile techniques, enabling effective mitigation of foreground contamination and improved handling of complex dust structures in the Galactic plane, which thus can provide more accurate extinction estimates, particularly in highly obscured regions. By applying XPNICER to the Galactic Plane Survey from the UKIRT Infrared Deep Sky Survey, we have generated a series of two-dimensional dust extinction maps that span roughly ∼1800 deg^2 of the Galactic plane ($0^\circ \lesssim l \lesssim 110^\circ$ and $140^\circ \lesssim l \lesssim 232^\circ$, $|b| \lesssim 5^\circ$). These maps, with spatial resolutions between 30 and 300 arcsec, can trace extinction up to $A_V \sim 30$–40 mag. This new approach offers higher spatial resolution and better detection of high-extinction regions compared to previous large-scale dust-based maps of the Galactic plane, providing an independent and complementary measure of dust column densities.

Key words: dust, extinction – Galaxy: structure – infrared: ISM – infrared: stars.

1 INTRODUCTION

Dust plays a crucial role in the interstellar medium (ISM), acting as an important tracer for Galactic ISM and offering insights into its physical properties. The spatial distribution of Galactic dust has been mapped using various data sets. Dust emission is a widely used method for mapping dust distribution on large scales. It has been used to construct several widely referenced all-sky dust maps that play an important role in many areas of astrophysical research (D. J. Schlegel, D. P. Finkbeiner & M. Davis 1998; Planck Collaboration XI 2014). However, converting thermal dust emission into dust column density involves assumptions about dust emissivity and the temperature distribution along the line of sight. These assumptions introduce significant uncertainties due to limited knowledge of the physical properties of interstellar dust (V. Ossenkopf & T. Henning 1994; B. T. Draine 2009; P. Padoan et al. 2014).

Another commonly used method involves measuring reddening towards many stars and treating them as individual samples of a continuous dust distribution. The extinction affecting a single star can be estimated by comparing its observed spectral energy distribution (SED) with its intrinsic SED. Although this approach ideally requires detailed spectroscopic data for accurate intrinsic characterization, it has the advantage of being independent of assumptions regarding dust temperature and physical properties. Consequently, this approach avoids the stringent assumptions about dust properties, which makes it a valuable complementary technique for tracing column density compared to methods based on thermal dust emission or gas tracers like ^{13}CO (B. T. Draine 2009; A. A. Goodman, J. E. Pineda & S. L. Schnee 2009; P. Padoan et al. 2014).

Many optical studies have focused on determining stellar parameters, distances, and reddening by using wide-field optical surveys and stellar evolutionary models (G. M. Green et al. 2019; Y. Bai et al. 2020; A. B. A. Queiroz et al. 2020; X. Zhang, G. M. Green & H.-W. Rix 2023). These studies generate catalogues that facilitate mapping of the three-dimensional (3D) distribution of dust (S. Rezaei Kh. et al. 2018; B. Q. Chen et al. 2019; G. M. Green et al. 2019; R. Lallement et al. 2019; R. H. Leike, M. Glatzle & T. A. Enßlin 2020; G. Edenhofer et al. 2024). However, dust maps from optical surveys struggle to capture high column density regions, which are essential for understanding star formation (Y. Gao & P. M. Solomon 2004; C. J. Lada, M. Lombardi & J. F. Alves 2010; M. Zhang et al. 2019). Since extinction decreases with longer wavelengths, near-infrared (NIR) data offer a broader dynamic range for measuring dust column density (C. J. Lada et al. 1994; K. Dobashi 2011; M. Juvela & J. Montillaud 2016). However, the lack of extensive NIR spectroscopic and astrometric surveys makes it challenging to obtain accurate stellar parameters. NIR extinction is usually determined by comparing observed NIR colours with average intrinsic ones, benefiting from the low variation in intrinsic colours and extinction laws at NIR wavelengths (J. A. Cardelli, G. C. Clayton & J. S. Mathis 1989; M. Lombardi & J. Alves 2001; S. Wang & B. W. Jiang 2014; S. Meingast, J. Alves & M. Lombardi 2018; S. Wang & X. Chen 2019; R. E. Butler & S. Salim 2024).

★ E-mail: miaomiao@pmo.ac.cn

© The Author(s) 2025.
Published by Oxford University Press on behalf of Royal Astronomical Society. This is an Open Access article distributed under the terms of the Creative Commons Attribution License (https://creativecommons.org/licenses/by/4.0/), which permits unrestricted reuse, distribution, and reproduction in any medium, provided the original work is properly cited.

Downloaded from https://academic.oup.com/mnras/article/543/4/3830/8276728 by guest on 30 October 2025

Various two-dimensional (2D) extinction mapping methods, including NICE (C. J. Lada et al. 1994), NICER (M. Lombardi & J. Alves 2001), PNICER (S. Meingast, M. Lombardi & J. Alves 2017), XNICER (M. Lombardi 2018), and Xpercentile (K. Dobashi et al. 2008), have been developed with distinct approaches. These techniques are commonly used to study column density structures in nearby star-forming regions (e.g. J. Kainulainen, K. Lehtinen & J. Harju 2006; M. Lombardi, J. Alves & C. J. Lada 2006; J. Kainulainen et al. 2007, 2009; M. Lombardi, C. J. Lada & J. Alves 2008, 2010; J. Alves, M. Lombardi & C. J. Lada 2014; A. Spilker, J. Kainulainen & J. Orkisz 2021). However, they are rarely applied to Galactic plane studies, as they are based on measuring the reddening of stars behind dust clouds, which becomes difficult in the Galactic plane due to the complex geometry of stars and dust (e.g. M. Lombardi 2005; J. Kainulainen et al. 2011; M. Juvela & J. Montillaud 2016; M. Zhang & J. Kainulainen 2022). Furthermore, the selection of suitable control fields for estimating intrinsic stellar colours becomes increasingly challenging in the Galactic plane, where most regions are affected by variable extinction.

To address this challenge, we have developed the NIR extinction mapping technique XPNICER (M. Zhang & J. Kainulainen 2022), building on PNICER (S. Meingast et al. 2017) and Xpercentile (K. Dobashi et al. 2008). XPNICER estimates stellar intrinsic colours using precise extinction data from *Gaia*, eliminating the need for nearby extinction-free reference fields. It also minimizes foreground contamination by selecting the reddest Xpercentile stars as background sources. This method is particularly effective in measuring extinction toward distant and/or dense dust clouds behind many foreground stars. We have applied XPNICER to the Vista Variables in the Vía Láctea (VVV) survey photometric data (D. Minniti et al. 2010; M. Zhang & J. Kainulainen 2019), creating a 2D extinction map covering the entire VVV survey area in the Galactic plane.

In this study, we extended the use of XPNICER to the UKIRT Infrared Deep Sky Survey (UKIDSS; A. Lawrence et al. 2007) Galactic Plane Survey (GPS; P. W. Lucas et al. 2008). We have derived 2D extinction maps with spatial resolutions from 30 to 180 arcsec, covering the entire UKIDSS/GPS region, with a dynamic range up to $A_V \sim 30$–40 mag. Section 2 outlines the source catalogues, including UKIDSS/GPS and *Gaia* Data Release 3 (DR3), while Section 3 reviews the XPNICER technique. Section 4 presents the extinction maps, and Section 5 compares them with several previous dust-based maps. The main findings are summarized in Section 6.

2 DATA

The UKIDSS/GPS catalogue provides measurements of the observed colours of sources within the Galactic plane. A key step in our XPNICER method involves estimating the intrinsic colours of these sources. To achieve this, we incorporated the *Gaia* DR3 data set, which enables a statistical estimation of the intrinsic colours of UKIDSS/GPS sources by dereddening their observed colours using precise extinction measurements from *Gaia* DR3.

2.1 The UKIDSS/GPS catalogue

The UKIDSS/GPS survey (P. W. Lucas et al. 2008) covers portions of the northern Galactic plane ($0^\circ \lesssim l \lesssim 110^\circ$ and $140^\circ \lesssim l \lesssim 232^\circ$; $|b| \lesssim 5^\circ$), utilizing the J, H, K filters with the UKIRT Wide Field Camera (M. Casali et al. 2007). UKIDSS/GPS provides arcsecond-scale spatial resolution and achieves median 5σ depths of $J = 19.77$, $H = 19.00$, and $K = 18.05$ mag (A. Lawrence et al. 2007). Additional information about the photometric system, calibration, and data processing can be found in P. C. Hewett et al. (2006), S. T. Hodgkin et al. (2009), M. J. Irwin (2008), and N. C. Hambly et al. (2008). For this study, we use the point source catalogue from the UKIDSS/GPS Data Release 11 Plus,[1] which includes observations collected between 2005 May and 2013 December. We selected point sources using an SQL query with the condition `mergedClass` $= -1$ or -2, following the recommendation of P. W. Lucas et al. (2008). To ensure data reliability, we further filtered the sources by requiring `ppErrbits` < 256, effectively removing detections with known issues. In addition, we applied a photometric uncertainty threshold of 0.35 mag in the J, H, and K_s bands to remove detections with unreasonably large errors. To correct for saturation, sources brighter than $J < 13.25$, $H < 12.75$, or $K < 12.0$ mag were replaced with photometric data from the Two Micron All Sky Survey (2MASS; M. F. Skrutskie et al. 2006) point source catalogue. As a result, we obtained approximately 426 million NIR sources within the UKIDSS/GPS survey region, with a median source number density of about 30 arcmin^{-2}. This is nearly twice the density of optical point sources detected in the Panoramic Survey Telescope and Rapid Response System Telescope #1 (Pan-STARRS1; K. C. Chambers et al. 2016). A detailed comparison of source number densities between the UKIDSS/GPS and Pan-STARRS1 surveys is provided in Appendix A.

2.2 *Gaia* DR3

Gaia DR3[2] is based on observations collected over the first 34 months of the *Gaia* mission (Gaia Collaboration 2016). DR3 provides highly precise parallax measurements, proper motions, and consistently derived multiwavelength photometry for around 1.8 billion sources. Additionally, this release includes a wide range of data products, such as spectroscopic observations, photometric time series, and numerous astrophysical parameters. For this study, we specifically use the astrophysical parameter catalogues from *Gaia* DR3.

The astrophysical data products in *Gaia* DR3 were generated using 13 distinct modules, each part of the astrophysical parameters inference system (apsis; O. L. Creevey et al. 2023; M. Fouesneau et al. 2023). For this study, we specifically use the catalogue produced by one of these modules, the General Stellar Parametrizer from Photometry (GSP-Phot; R. Andrae et al. 2023). This catalogue was derived from a combination of *Gaia*'s astrometry, photometry, and low-resolution BP/RP (Blue Photometer/Red Photometer) spectra. GSP-Phot employed a Bayesian forward-modelling approach to create a homogeneous catalogue that includes estimates of stellar parameters, distances, and extinctions for roughly 471 million sources with magnitudes of $G < 19$. For bright sources, the typical uncertainty in extinction (A_G) is about 0.06 mag. Further details on *Gaia* DR3 are provided in Gaia Collaboration (2023) and C. Babusiaux et al. (2023).

To exclude spurious astrometric data from the *Gaia* DR3 catalogue, we apply the approach outlined by J. Rybizki et al. (2022). This method classifies astrometric solutions into 'good' and 'bad' categories, using the *Gaia* Early Data Release 3 data set as a training set. A machine learning-based parameter, termed 'astrometric fidelity', is introduced to identify spurious sources. Compared to traditional quality checks that rely on parameters like `ruwe`, the 'astrometric

[1] http://wsa.roe.ac.uk/dr11plus_release.html
[2] https://gea.esac.esa.int/archive/

Downloaded from https://academic.oup.com/mnras/article/543/4/3830/8276728 by guest on 30 October 2025

fidelity' parameter offers a more refined selection of sources with reliable astrometric solutions. Additionally, J. Rybizki et al. (2022) provided a method for evaluating photometric contamination from nearby sources (`norm_dg`). The following criteria from J. Rybizki et al. (2022) are therefore applied to filter out sources with unreliable astrometric data or anomalous colours in *Gaia* DR3:

$$\texttt{fidelity_v2} > 0.5, \tag{1}$$

$$\texttt{norm_dg} = \texttt{nan} \text{ or } \texttt{norm_dg} < -3. \tag{2}$$

Finally, we obtained about 63 million *Gaia* DR3 sources with GSP-Phot extinction estimates within the UKIDSS/GPS survey region. After applying the filtering criteria described in equations (1) and (2), about 52 million sources with relatively reliable extinction estimates remain. It is important to note that these 'reliable' GSP-Phot extinction estimates are not suitable for precise measurements of individual stars, but are more appropriately used for statistical analyses of large stellar samples, such as extinction mapping (R. Andrae et al. 2018). Recent studies have also published extinction estimates based on the *Gaia* DR3 data base using alternative models and algorithms (A. B. A. Queiroz et al. 2023; H. Zhao et al. 2024). While these results are generally consistent in a statistical sense, systematic differences exist among them. One well-known limitation of the GSP-Phot parameters is the tendency to overestimate both effective temperature and extinction for sources with visual extinction $A_V \gtrsim 2$ mag, due to the degeneracy between temperature and extinction (R. Andrae et al. 2023; H. Zhao et al. 2024). This issue introduces a zero-point bias in our extinction maps. We attempted to correct this zero-point offset by comparing our XPNICER extinction estimates with those from an external catalogue offered by X. Zhang et al. (2023) (see Section 4.1 for details). It is important to note that extinction catalogues based on *Gaia* XP spectra, such as X. Zhang et al. (2023), offer higher precision but are limited to brighter sources, resulting in sparse coverage, especially in heavily obscured regions. Our choice of the *Gaia* DR3 GSP-Phot catalogue reflects a trade-off between its comprehensive spatial coverage, which is critical for this work, and the higher precision of the sparser X. Zhang et al. (2023)'s catalogue.

2.3 Combined catalogue as input of extinction mapping

A combined catalogue was produced by merging the UKIDSS/GPS point source catalogue (see Section 2.1) with the astrophysical parameters catalogue from *Gaia* DR3 (see Section 2.2), applying a matching tolerance of 0.5 arcsec. In this work, we did not account for source proper motions during the cross-matching process, as propagating *Gaia* astrometry to the UKIDSS/GPS observational epoch for each individual source is computationally complex. To evaluate the potential impact of this simplification, we compared our directly matched catalogue with the external cross-matched catalogue XGAPS (cross-match of Galactic Plane Surveys; S. Scaringi et al. 2023). We found that the contamination of mismatches did not affect the statistical properties of the NIR intrinsic colours of matched sources. A detailed comparison is presented in Appendix B. Based on this assessment, we chose to adopt the merged catalogue without applying proper motion corrections. This merged data set was subsequently used as input for our extinction mapping process, outlined in Section 3. In the combined catalogue, around ∼12 per cent of NIR sources have *Gaia* GSP-Phot extinction estimates.

3 METHOD

The comprehensive explanation of the XPNICER method is available in M. Zhang & J. Kainulainen (2022). In this section, we present an overview of this technique and its application to the UKIDSS/GPS point source catalogue. XPNICER, briefly, combines the PNICER (S. Meingast et al. 2017) and Xpercentile (K. Dobashi et al. 2008) approaches. Specifically, it estimates the extinction for individual stars by comparing their observed colours with statistically inferred intrinsic colours from *Gaia* GSP-Phot sources in the same region. Next, stars are grouped into discrete sightlines, and potential background sources along different lines of sight are identified using the Xpercentile method. These background stars are then used to map the spatial distribution of integrated dust extinction.

3.1 Extinction estimation towards single star

In our input catalogue (Section 2.3), around 50 million sources have *Gaia* DR3 extinction measurements. For each source, extinction data from *Gaia* DR3 were supplied as a median value along with associated confidence intervals. To simplify the analysis and manage asymmetrical errors, we transformed these intervals into a symmetric standard deviation, assuming Gaussian error distribution. For UKIDSS/GPS sources without *Gaia* DR3 extinction measurements, extinction values were estimated using the PNICER method. Specifically, the UKIDSS/GPS survey area was divided into multiple subregions, and extinction for sources lacking *Gaia* DR3 estimates ($A_{V,\mathrm{PNICER}}^{*\,\mathrm{control:\,}Gaia\,\mathrm{DR3}}$)[3] was determined by comparing their observed colours to dereddened colours of sources with *Gaia* DR3 measurements within the same subregion, following the extinction law from S. Wang & X. Chen (2019). The sizes of subregions range from $0.5^\circ \times 0.5^\circ$ to $4^\circ \times 4^\circ$, in increments of 0.5°. This means that for each star, a series of extinction estimates is obtained based on varying subregion sizes. The final extinction value for each star is adopted as the median of these estimates. This averaging procedure is designed to mitigate the tile effect caused by any particular subregion size. S. Wang & X. Chen (2019) examined the extinction law from optical to mid-infrared (MIR) wavelengths for a sample of red clump stars identified through stellar parameters provided by the APOGEE (Apache Point Observatory Galactic Evolution Experiment) survey. They measured relative extinction across numerous passbands from surveys, such as *Gaia*, 2MASS, and *WISE* (*Wide-field Infrared Survey Explorer*), indicating an average extinction law in the NIR that is steeper than the commonly used CCM (Cardelli–Clayton–Mathis) model (J. A. Cardelli et al. 1989). The uncertainties in $A_{V,\mathrm{PNICER}}^{*\,\mathrm{control:\,}Gaia\,\mathrm{DR3}}$ are mainly due to photometric errors and variations in intrinsic colours.

However, the selection of UKIDSS/GPS point sources with *Gaia* DR3 extinction estimates as reference stars was biased toward nearby and bright stars, introducing additional uncertainties in the PNICER extinction estimates. To assess these uncertainties, we used the Besançon model for Galactic stellar population synthesis (A. C. Robin et al. 2003), as suggested by M. Zhang & J. Kainulainen (2022). For each $1^\circ \times 1^\circ$ subregion, we focused on a 30 arcmin × 30 arcmin central area and extracted pseudo-stars from the Besançon model. Using linear extinction relations with distance, we created synthetic colour–colour diagrams and colour–magnitude diagrams. The best-fitting model was identified by minimizing differences between observed and synthetic star density maps in the colour

[3]For clarity, in the following context, we refer to the extinctions of stars as A_V^* and the extinction values of the extinction map as A_V.

Downloaded from https://academic.oup.com/mnras/article/543/4/3830/8276728 by guest on 30 October 2025

space. Extinctions for UKIDSS/GPS point sources ($A_{V,\mathrm{PNICER}}^{*\,\mathrm{control:\,Besançon}}$) were then calculated using the PNICER method, with pseudo-stars from the optimized Besançon model serving as reference stars. The standard deviation ($\sigma_{\Delta A_V^*}$) of the extinction difference $\Delta A_V^* = A_{V,\mathrm{PNICER}}^{*\,\mathrm{control:\,Besançon}} - A_{V,\mathrm{PNICER}}^{*\,\mathrm{control:}\,Gaia\,\mathrm{DR3}}$ quantified the extra uncertainty caused by biased reference stars. To reduce edge effects, we smoothed the $\sigma_{\Delta A_V^*}$ map using a Gaussian kernel. The total uncertainty (σ_{total}) for A_V^* in UKIDSS/GPS sources without *Gaia* DR3 extinction estimates combined the PNICER method error (σ_{PNICER}) with the bias-induced uncertainty ($\sigma_{\Delta A_V^*}$). In the above process, we did not account for the systematic offset in ΔA_V^*, as it strongly depends on the assumed dust distribution along the line of sight and is difficult to quantify without detailed knowledge of the 3D dust structure. However, this systematic offset does affect the zero-point of our extinction map. We attempt to estimate this zero-point offset using a data-driven approach in Section 4.1.

3.2 Extinction mapping with potential background sources

To select background sources and map the integrated Galactic extinction, we employed the 'Xpercentile method' as described by K. Dobashi et al. (2008). The full application of this approach within XPNICER is detailed by M. Zhang & J. Kainulainen (2022); here, we provide a brief overview. The UKIDSS/GPS survey region was divided into square sightline cells. These grid cells varied in size from 30 to 180 arcsec, where smaller cells improved spatial resolution at the expense of increased noise, and larger cells reduced noise but sacrificed resolution.

We then sorted the UKIDSS/GPS point sources within each grid cell according to their A_V^* values in ascending order. The qth percentile of A_V^* was labelled as $A_V^*(q)$. By defining the X_0th and X_1th percentiles ($0 \leq X_0 < X_1 \leq 100$ per cent) of A_V^* as $A_V^*(X_0)$ and $A_V^*(X_1)$, respectively, we selected the UKIDSS/GPS point sources within each grid cell that fall within $A_V^*(X_0) \leq A_V^* \leq A_V^*(X_1)$ as background sources. Following the approach outlined by M. Zhang & J. Kainulainen (2022), we chose $X_0 = 80$ per cent for background source selection and $X_1 = 95$ per cent to exclude sources with significant infrared excess. However, for distant and/or dense dust clouds, the $X_0 = 80$ per cent threshold might not adequately identify true background sources. Therefore, we also used an $X_0 = 90$ per cent threshold, but only for larger grid cells ($\geqslant$60 arcsec). We note that adopting a threshold of $X_1 = 95$ per cent is relatively conservative. M. Zhang & J. Kainulainen (2022) estimated the fraction of young stellar objects (YSOs) along various lines of sight based on the YSO sample identified by M. Zhang et al. (2019), and found that the YSO fraction can reach up to $\sim$1 per cent in regions of dense gas due to YSO clustering. While using $X_1 = 95$ per cent may exclude some reddened background sources, it effectively removes sources with infrared excess.

Finally, we employed a Gaussian kernel to smooth the A_V^* values of the selected background sources, producing the extinction maps. The full width at half-maximum (FWHM) of the Gaussian kernels was set to match the size of the grid cells, while the pixel size of the extinction map was half the FWHM of the kernel. The Gaussian kernel is defined based on the positions and extinction uncertainties of the background sources. In this work, we did not apply corrections for the bias in extinction measurements caused by small-scale cloud substructures (M. Lombardi 2009). To estimate the uncertainties of the extinction maps, we used a Monte Carlo approach. This method involved assuming Gaussian error distributions for the A_V^* values of the UKIDSS/GPS point sources. We generated random

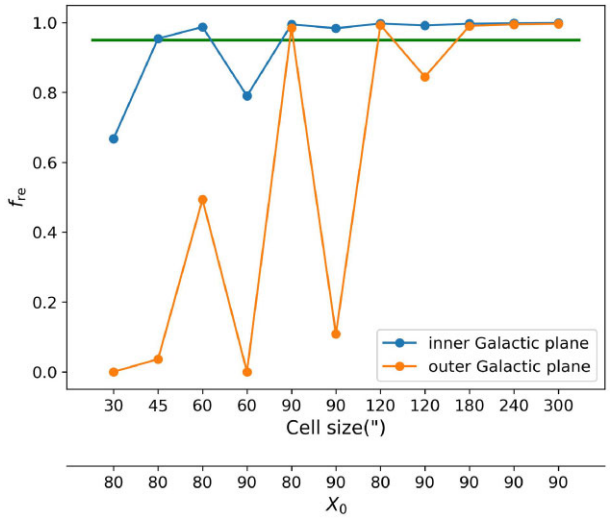

Figure 1. The fraction of reliable cells relative to the total number of cells, denoted as f_{re}, is presented for various cell sizes and X_0 configurations in the extinction maps of both the inner and outer Galactic plane. A horizontal solid line marks the threshold of $f_{\mathrm{re}} = 0.95$. Extinction maps with f_{re} values below this threshold are considered unreliable, as they contain an insufficient number of background sources in some beams.

A_V^* values for each point source to create a simulated UKIDSS/GPS catalogue. These simulated sources were then organized into a grid, and background sources were selected within each grid cell using the XPNICER technique described earlier. The extinction maps were produced by applying the Gaussian kernel to the A_V^* values of the simulated background sources. This simulation was repeated 10 times, yielding 10 extinction maps. The average of these maps and their standard deviation were used to determine the final extinction map and its associated uncertainty map.

4 RESULTS

4.1 Dust extinction maps and associated uncertainties

We generated extinction maps, along with corresponding uncertainty and background source number density maps, for both the inner ($l \sim 0°$–$110°$) and outer ($l \sim 140°$–$232°$) Galactic plane. Two sets of maps were produced: one with spatial resolutions of 30, 45, 60, 90, and 120 arcsec using a percentile configuration of $X_0 = 80$ per cent and $X_1 = 95$ per cent, and another with resolutions of 60, 90, 120, 180, 240, and 300 arcsec using $X_0 = 90$ per cent and $X_1 = 95$ per cent. For clarity, we adopt a shorthand notation for the maps throughout the paper. For example, the extinction map with 90 arcsec resolution and $X_0 = 80$ per cent is denoted as $A_V^{90}(X_0 = 80)$; its associated uncertainty and background source number density maps are denoted as $\delta A_V^{90}(X_0 = 80)$ and $N_{\mathrm{bg}}^{90}(X_0 = 80)$, respectively.

Cells containing three or more background sources are considered reliable. For each extinction map, we define the reliability fraction, f_{re}, as the ratio of reliable cells to the total number of cells, varying with resolution and X_0 configuration. Fig. 1 shows f_{re} for different extinction maps across various resolutions and X_0 values. For example, the inner and outer Galactic plane extinction maps with 60 arcsec resolution and $X_0 = 80$ per cent have f_{re} values of 0.99 and 0.49, respectively. This means that at least three background sources are present in 99 per cent of the beams in the inner region and 49 per cent in the outer region for the map $A_V^{60}(X_0 = 80)$.

Downloaded from https://academic.oup.com/mnras/article/543/4/3830/8276728 by guest on 30 October 2025

We propose a rough reliability level of 0.95 for $f_{\rm re}$, suggesting that the extinction maps $A_V^{30}(X_0 = 80)$, $A_V^{45}(X_0 = 80)$, and $A_V^{60}(X_0 = 90)$ for the inner Galactic plane, extinction maps with resolution of <90 arcsec, $A_V^{90}(X_0 = 90)$, and $A_V^{120}(X_0 = 90)$ for the outer Galactic plane are unreliable due to the insufficient number of background sources in some beams. Therefore, although we have released all extinction maps with various resolutions and configurations in Section 2.1, we recommend that readers only use the reliable maps. Specifically, maps with a resolution of 60 arcsec or higher – excluding $A_V^{60}(X_0 = 90)$ – should be used for the inner Galactic plane, and maps with a resolution of 90 arcsec or higher – excluding $A_V^{90}(X_0 = 90)$ and $A_V^{120}(X_0 = 90)$ – should be used for the outer Galactic plane. It should be noted that the reliability threshold we propose is not a strict or universally applicable limit. Users may define their own reliability criteria based on scientific requirements, using the released background source number density maps as a reference.

We also released an uncertainty map associated with each extinction map. The uncertainty maps primarily include contributions from observed photometric uncertainties, variations in intrinsic colours, and biases in reference sources. However, as noted by M. Zhang & J. Kainulainen (2022), the uncertainty maps do not account for systematic uncertainties, such as zero-point errors and uncertainties due to extinction laws.

The zero-point offset in our extinction maps mainly originates from two sources. First, there are systematic biases in the *Gaia* GSP-Phot extinction estimates due to the degeneracy between stellar temperature and extinction (see Section 2.2). Second, systematic errors can arise from the use of reference sources. Since *Gaia* extinction measurements are only available for relatively bright stars, using their intrinsic colours to estimate the intrinsic colours of fainter background stars may introduce additional biases (see Section 3.1). To assess the zero-point offset, we employed a reference catalogue that provides extinction estimates ($A^*_{V,\,\rm Zhang2023}$) and other stellar parameters for ∼220 million stars. These parameters were derived from *Gaia* XP spectra using a data-driven approach (X. Zhang et al. 2023).

Compared to the GSP-Phot extinction estimates, X. Zhang et al. (2023) focused on *Gaia* sources with XP spectra and adopted an empirical forward modelling approach that is independent of any stellar evolutionary models. This methodology enables more accurate and robust extinction estimation. To select high-quality extinction measurements from the catalogue of X. Zhang et al. (2023), we applied the following criteria:

$$\begin{aligned} \texttt{quality_flags} &< 8, \\ E &\leq 10, \\ \sigma_E &\leq 0.04, \\ \sigma_\omega/\omega &< 0.1, \end{aligned}$$

where E and ω are the extinction and parallax of sources, respectively, while σ_E and σ_ω are the associated uncertainties. Here, E is actually a scalar proportional to extinction, which can be converted to $A^*_{V,\,\rm Zhang2023}$ value using a extinction curve. We further required $\omega < 0.2$ mas to select sources located at large distances of $\gtrsim$5 kpc, yielding ∼0.5 million sources within the UKIDSS/GPS survey area. For each source with an extinction measurement $A^*_{V,\,\rm Zhang2023}$, we extracted its corresponding extinction $A^*_{V,\rm XPNICER}$ from our XPNICER extinction map based on its Galactic coordinates. The extinction difference was defined as $Z_0^* = A^*_{V,\rm XPNICER} - A^*_{V,\,\rm Zhang2023}$. We then applied a σ-clipping algorithm to remove outliers in the Z_0^* distribution. Finally, the zero-point offset map Z_0 was constructed by smoothing Z_0^* with a Gaussian kernel of FWHM = 1°.

Fig. 2 shows the Z_0 map whose values span from 0.2 to 4.5 mag with a median value of ∼3 mag. Obviously, Z_0 is the function of the Galactic positions. On average, Z_0 of the inner Galactic plane is higher than that of the outer Galactic plane as well as Z_0 has higher values in some high extinction regions. We note that the median value (∼3 mag) of the Z_0 map is significantly higher than the zero-point offset (∼1 mag) derived by M. Zhang & J. Kainulainen (2022). However, M. Zhang & J. Kainulainen (2022) compared their map with *Planck* dust map (Planck Collaboration XI 2014) and found that their XPNICER extinction systematically overestimated the A_V value of about 3–4 mag. Therefore, we believed that M. Zhang & J. Kainulainen (2022) should underestimate the zero-point offset of their extinction map.

The systematic uncertainties arising from extinction laws have been thoroughly discussed by M. Zhang & J. Kainulainen (2022). Generally speaking, our study assumes a universal NIR extinction law for the entire UKIDSS/GPS survey area, as proposed by S. Wang & X. Chen (2019). This law, characterized by $\alpha = 2.07 \pm 0.03$, follows a power-law relation $A_\lambda \propto \lambda^{-\alpha}$. Although other studies suggest different α values, from 1.61 to 2.47 (G. H. Rieke & M. J. Lebofsky 1985; J. Alonso-García et al. 2017; J. Hosek et al. 2018; J. L. Sanders et al. 2022), the variation introduces uncertainties in extinction estimation as discussed by M. Zhang & J. Kainulainen (2022). Large-scale investigations generally support a universal NIR extinction law, but specific environments like star-forming regions may exhibit different laws (S. Wang et al. 2013; S. Wang & B. W. Jiang 2014; S. Meingast et al. 2018; J. Maíz Apellániz et al. 2020). Our chosen α value results in uncertainties of within 3 per cent for visual extinctions, though systematic errors could reach 20–30 per cent as suggested by M. Zhang & J. Kainulainen (2022).

Fig. 2 also presents the $A_V^{90}(X_0 = 90)$, $\delta A_V^{90}(X_0 = 80)$, and $N_{\rm bg}^{90}(X_0 = 80)$ for both the inner and outer area of the Galactic plane, as surveyed by UKIDSS/GPS in units of A_V. Here we emphasized that the zero-point offset (Z_0) has been subtracted from the extinction map ($A_V^{90}(X_0 = 90)$). In the subsequent context, $A_V^{\rm FWHM}(X_0)$ denotes the zero-point corrected extinction maps. Fig. C1 shows a close view of $A_V^{90}(X_0 = 80)$, revealing amounts of detailed dust structures in the Galactic plane.

Some tile patterns are visible in the extinction, uncertainty, and source number density maps, particularly in the outer Galactic plane regions. These patterns likely result from varying sensitivity across the UKIDSS/GPS survey, as noted by M. Zhang & J. Kainulainen (2022), and can be removed by applying a brightness cut to the background sources (see Appendix D for details). However, imposing such a cut would significantly reduce the number of background sources, thereby decreasing the resolution and dynamic range of the extinction maps. For this reason, we chose not to correct for the tile pattern effect.

4.2 Limiting distance corresponding to integrated extinction

By design, our extinction maps are sensitive to extinction integrated to a limiting distance, $d_{\rm limit}$, along the line of sight. This $d_{\rm limit}$ is clearly dependent on Galactic longitude and latitude, as well as the detection limit of the UKIDSS/GPS survey and the 3D dust distribution. We first made rough estimates of the range where $d_{\rm limit}$ might fall. For these estimates, we divided the UKIDSS/GPS coverage area into $1^\circ \times 1^\circ$ subregions. In each subregion, we used the 99.5th percentile of K-band magnitudes as the detection limit. Assuming a constant dust distribution profile of $A_V \sim 0.75$ mag kpc^{-1} (G. Lynga 1982),

Downloaded from https://academic.oup.com/mnras/article/543/4/3830/8276728 by guest on 30 October 2025

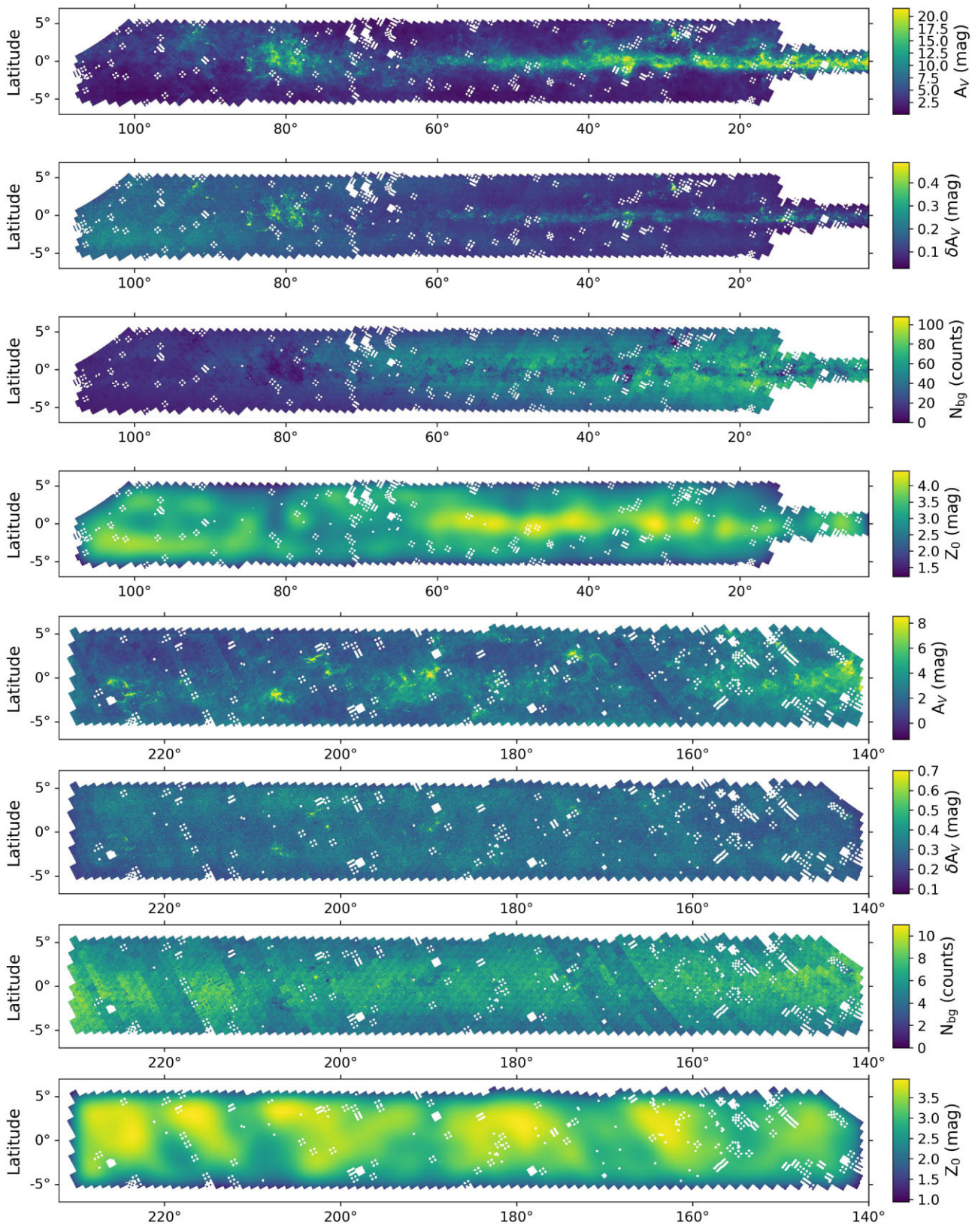

Figure 2. The XPNICER extinction maps, associated uncertainty maps, number density maps of background sources, and zero-point offset map obtained using $X_0 = 80$ per cent and $X_1 = 95$ per cent with the spatial resolution of 90 arcsec for the Galactic plane area covered by UKIDSS/GPS. The zero-point offset has been subtracted from the extinction map.

Downloaded from https://academic.oup.com/mnras/article/543/4/3830/8276728 by guest on 30 October 2025

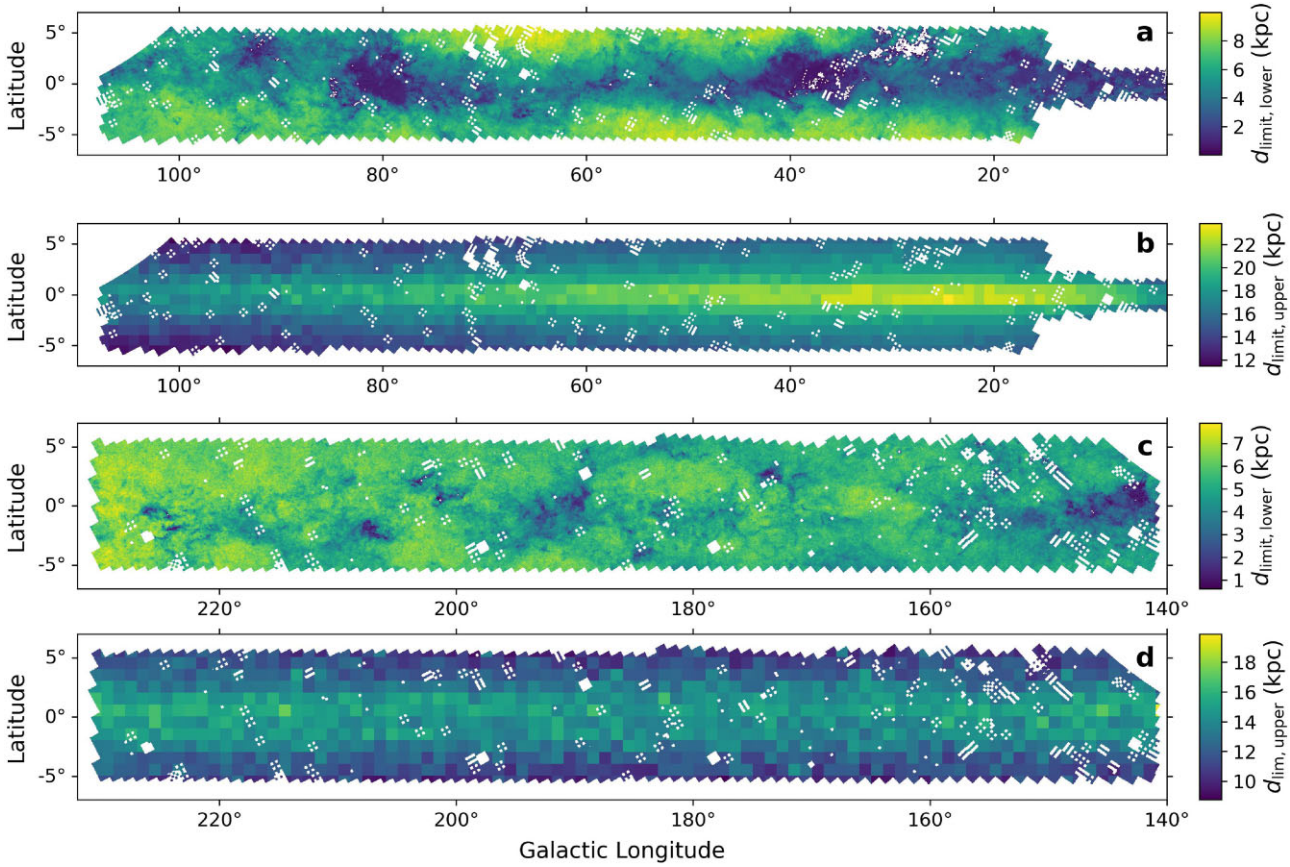

Figure 3. The upper and lower limit of the limiting distance ($d_{\rm limit}$) to which the extinction integrated. Panels (a) and (c) show the lower limit ($d_{\rm limit,\,lower}$) map of the inner and outer Galactic plane, respectively. Panels (b) and (d) present the upper limit ($d_{\rm limit,\,upper}$) map of the inner and outer Galactic plane.

we estimated $d_{\rm limit,upper}$ for each detection limit using the TRILEGAL[4] model (L. Girardi et al. 2005). TRILEGAL is a stellar population synthesis code that simulates the stellar photometry of any Galactic field. Thus, the UKIDSS/GPS survey can detect stars up to $d_{\rm limit,upper}$ along different sightlines, considering only a simple model for the diffuse dust distribution in the Galaxy. Figs 3(b) and (d) show the spatial distribution maps of $d_{\rm limit,upper}$, representing the upper limit of $d_{\rm limit}$. We found that $d_{\rm limit,upper}$ varies from ∼10 to ∼20 kpc among different sightlines.

Since extinction decreases with increasing wavelength, more background stars can be detected at longer wavelengths, such as in NIR. Detecting more distant background stars along a given line of sight implies that the extinction can be integrated out to a larger limiting distance ($d_{\rm limit}$). C. J. Lada et al. (1994) demonstrated that NIR extinction maps can trace dust column densities with a dynamic range several times greater than that of optical extinction maps, indicating that NIR-based maps typically have higher $d_{\rm limit}$ values. Therefore, we can infer a lower limit for $d_{\rm limit}$ (denoted as $d_{\rm limit,lower}$) by using a published 3D extinction map derived from optical surveys. G. M. Green et al. (2019) constructed a 3D dust extinction map of the northern sky (Dec. $> -30^\circ$) using data from *Gaia* Data Release 2 (DR2), Pan-STARRS1 (K. C. Chambers et al. 2016), and 2MASS. They determined distances, reddenings, and stellar parameters for approximately 799 million stars, mapping the Galactic dust distribution at an angular scale ranging from 3.4 to 13.7 arcmin. G. M. Green et al. (2019) also defined the maximum reliable depth to which their map accurately traces dust. Compared to *Gaia*, Pan-STARRS1, and 2MASS, the UKIDSS/GPS survey detects significantly fainter and more distant stars. Therefore, the maximum reliable depth can be considered a conservative lower limit of $d_{\rm limit}$. Figs 3(a) and (c) show the spatial distribution map of $d_{\rm limit,lower}$, equivalent to the maximum reliable depth defined by G. M. Green et al. (2019). In the Galactic plane covered by UKIDSS/GPS, $d_{\rm limit,lower}$ ranges from approximately 1 to 10 kpc.

Although fully quantifying $d_{\rm limit}$ without a detailed 3D model of Galactic dust is not feasible, we provided a rough estimate based on the 3D extinction map by G. M. Green et al. (2019). Specifically, G. M. Green et al. (2019) presented visual extinction profiles as functions of distance for various sightlines. Figs 4(a)–(c) illustrate the relationships between extinction and distance along three sightlines. G. M. Green et al. (2019) defined the minimum ($d_{\rm min}$) and maximum reliable depths ($d_{\rm max} = d_{\rm limit,lower}$) for each sightline. However, the extinction profile actually extends over the maximum reliable depth and up to 63 kpc, although data beyond such a large distance are sparse. Thus, if our XPNICER extinction value ($A_{V,\rm XPNICER}$) intersects G. M. Green et al. (2019)'s extinction profile within the distance range [$d_{\rm limit,lower}$, $d_{\rm limit,upper}$], we set the intersection point's distance as $d_{\rm limit}$, as shown in Fig. 4(a). Otherwise, we assumed a linear dust model along each sightline:

$$A_V = aD, \tag{3}$$

where A_V and D are the visual extinction and distance, respectively. We fit G. M. Green et al. (2019)'s extinction profile in the range

[4] http://stev.oapd.inaf.it/cgi-bin/trilegal

Downloaded from https://academic.oup.com/mnras/article/543/4/3830/8276728 by guest on 30 October 2025

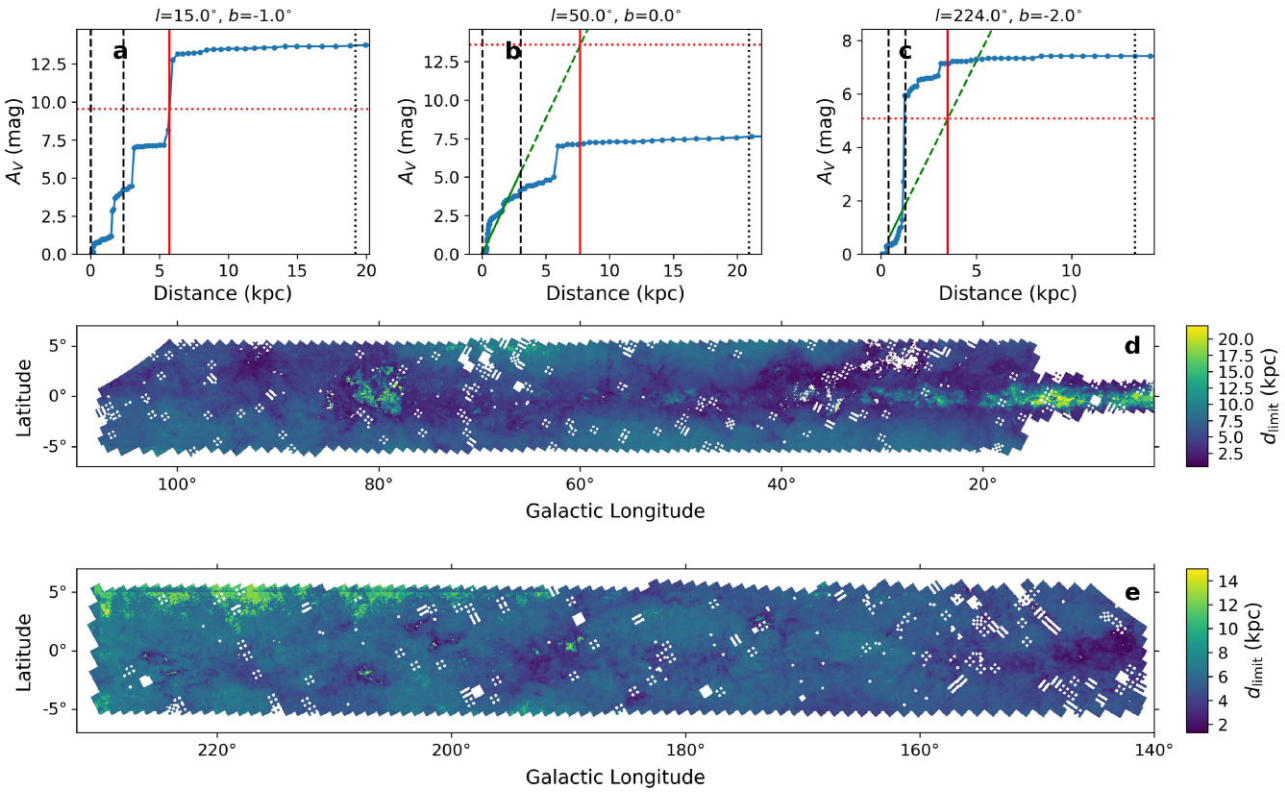

Figure 4. Panels (a), (b), and (c) display the visual extinction profiles as functions of distance for three sightlines from G. M. Green et al. (2019). The blue points and lines represent these extinction profiles. The minimum and maximum reliable depths (d_{min}, d_{max}) defined by G. M. Green et al. (2019) are indicated by black dashed vertical lines. Panels (a), (b), and (c) illustrate the method used to quantify d_{limit}. As described in the main text, we first estimate the lower and upper bounds of d_{limit}, denoted as $d_{limit,lower}$ and $d_{limit,upper}$, respectively. The lower limit ($d_{limit,lower} = d_{max}$) is indicated by a vertical black dashed line, while the upper limit is shown by a vertical black dotted line. The horizontal red dotted line represents the integrated extinction ($A_{V,XPNICER}$) from our XPNICER map along each sightline. In panel (a), the horizontal red dotted line intersects the extinction profile from G. M. Green et al. (2019) (shown in blue) within the range [$d_{limit,lower}$, $d_{limit,upper}$]. The distance at this intersection is taken as d_{limit} for that sightline and is marked with a vertical red solid line. In panels (b) and (c), no intersection occurs between $A_{V,XPNICER}$ and the extinction profiles within the specified range. In these cases, we fit the extinction profile between d_{min} and d_{max} (i.e. the section of the blue line bounded by the two vertical black dashed lines) using a linear dust model, as detailed in the main text. The resulting fits are shown as green solid and dashed lines. Where the green dashed line intersects the horizontal red dotted line, we adopt the corresponding distance as d_{limit}, again marked with a vertical red solid line. Panels (d) and (e) show the final d_{limit} map in the inner and outer Galactic plane, respectively.

[d_{min}, d_{max}] along each sightline using equation (3) with bounded constraints of [$(A_{V,XPNICER})/(d_{limit,upper})$, $(A_{V,XPNICER})/(d_{limit,lower})$] for the slope a. We then determined d_{limit} using $(A_{V,XPNICER})/a$, as shown in Figs 4(b) and (c). These bounded constraints ensured d_{limit} falls within [$d_{limit,lower}$, $d_{limit,upper}$].

Finally, we obtained the d_{limit} maps, shown in Figs 4(d) and (e) for the inner and outer Galactic plane. We found that d_{limit} ranged from ∼2 to 20 kpc. In some low-extinction regions dominated by diffuse dust, the limiting distance (d_{limit}) can reach ∼18–20 kpc, approaching the level of the 'total Galactic dust extinction'. Compared to our maps, previous large-scale NIR extinction maps, such as those by K. Dobashi (2011) and M. Juvela & J. Montillaud (2016), were unable to capture the full extent of extinction, primarily due to their underestimation of the contribution from diffuse dust components (M. Zhang & J. Kainulainen 2022). However, it is important to emphasize that the d_{limit} values presented here are rough estimates with large uncertainties. For example, some high-extinction regions near $b = 0°$ also show d_{limit} values of ∼20 kpc. This does not indicate that our extinction map fully traces the total dust column in these dense areas. Rather, it reflects the complexity of the dust distribution along these lines of sight, which cannot be described by a simple linear model.

5 DISCUSSION

In this section, we compare our newly developed XPNICER extinction map with several prior dust-based maps. Using VVV survey data, M. Zhang & J. Kainulainen (2022) produced an XPNICER extinction map of the southern Galactic plane and compared it with 10 pre-existing dust-based maps, including the all-sky 2D dust extinction maps (K. Dobashi 2011; M. Juvela & J. Montillaud 2016), opacity maps derived from dust emission (D. J. Schlegel et al. 1998; Planck Collaboration XI 2014; K. A. Marsh et al. 2017), and 3D dust extinction maps (M. Schultheis et al. 2014). They found overall consistency across all comparisons. Consequently, instead of repeating analyses with numerous maps, we limited our comparison here to three: our previous XPNICER map of the southern Galactic plane (M. Zhang & J. Kainulainen 2022), the commonly used *Planck* dust map (Planck Collaboration XI 2014), and the 3D extinction map by G. M. Green et al. (2019).

Downloaded from https://academic.oup.com/mnras/article/543/4/3830/8276728 by guest on 30 October 2025

The *Planck* dust map (Planck Collaboration XI 2014) is chosen as a representative of opacity maps based on dust emission. While the point process mapping (PPMAP) method, applied to the *Herschel* infrared Galactic Plane (Hi-GAL) survey (K. A. Marsh et al. 2017), provides dust maps with a higher spatial resolution (∼12 arcsec), it is limited in coverage to Galactic plane latitudes of $|b| \lesssim 1^{\circ}$. Furthermore, M. Zhang & J. Kainulainen (2022) found that due to inaccuracies in the absolute flux calibration of the Hi-GAL images, the zero-point of PPMAPs may lack uniformity, which complicates consistent, large-scale comparisons between PPMAPs and other dust maps.

We selected the 3D extinction map by G. M. Green et al. (2019) for comparison, as it aligns well with our XPNICER map in terms of coverage, spatial resolution, and sensitivity. Although numerous 3D dust extinction maps have been published, some feature low spatial resolutions ($\gtrsim$10 arcmin; D. J. Marshall et al. 2006; C. Hottier, C. Babusiaux & F. Arenou 2020; T. E. Dharmawardena et al. 2024), while others with high resolution are limited to tracing integrated dust distributions up to a small distance ($\lesssim$3 kpc; R. Lallement et al. 2019, 2022; R. H. Leike & T. A. Enßlin 2019; R. H. Leike et al. 2020; J. L. Vergely, R. Lallement & N. L. J. Cox 2022; G. Edenhofer et al. 2024). B. Q. Chen et al. (2019) also created a 3D dust reddening map with about 6 arcmin resolution across the entire Galactic plane, based on *Gaia* and 2MASS data. However, G. M. Green et al. (2019)'s map can trace dust densities to farther distances than B. Q. Chen et al. (2019)'s, benefiting from the deeper photometric data provided by Pan-STARRS1.

For simplicity, we refer to our XPNICER extinction map as A_V(XPNICER), and to the other dust-based maps by M. Zhang & J. Kainulainen (2022), Planck Collaboration XI (2014), and G. M. Green et al. (2019) as A_V(Zhang2022), A_V(*Planck*), and A_V(Green2019), respectively. It is important to note that the *Planck* dust map was originally obtained in units of optical depth, specifically τ_{353}(*Planck*), where τ_{353} represents the optical depth at a frequency of 353 GHz (∼850 μm). The colour excess $E(B-V)$ map was subsequently derived using a conversion factor from τ_{353} to $E(B-V)$, which was estimated based on extinction measurements of extragalactic objects by Planck Collaboration XI (2014). Finally, the A_V(*Planck*) map was obtained by applying the relation between A_V and $E(B-V)$ as suggested by E. F. Schlafly & D. P. Finkbeiner (2011).

We present visual comparisons of A_V(XPNICER) with the other maps in Section 5.1. Following that, we make quantitative pixel-to-pixel comparisons in Sections 5.2–5.4.

5.1 Visual comparison

Fig. 5 provided a close-up view of a section in the inner Galactic plane across the A_V(XPNICER), A_V(Zhang2022), A_V(*Planck*), and A_V(Green2019) maps. The A_V(Zhang2022) map was also constructed using the XPNICER mapping technique (M. Zhang & J. Kainulainen 2022). However, its zero-point was not corrected in the original work. Following the method described in Section 4.1, we computed a zero-point offset map for A_V(Zhang2022) and subtracted it to obtain a corrected extinction map. Then A_V(Zhang2022) was compared with A_V(XPNICER) under the same configuration of FWHM = 60 arcsec and $X_0 = 90$. This comparison revealed that both maps exhibit nearly identical extinction structures, though A_V(Zhang2022) appeared smoother than A_V(XPNICER). Actually, the average extinction uncertainties in A_V(XPNICER) and A_V(Zhang2022) were 0.24 and 0.12 mag, respectively, indicating that A_V(Zhang2022) possessed a higher signal-to-noise ratio. This is due to A_V(Zhang2022) being derived from a deep photometric catalogue obtained by performing point spread function (PSF) photometry on stacked multi-epoch VVV images (M. Zhang & J. Kainulainen 2019).

In comparison with A_V(*Planck*), our A_V(XPNICER) map under the configuration of FWHM = 90 arcsec and $X_0 = 80$, i.e. $A_V^{90}(X_0 = 80)$, offered higher spatial resolution, enabling the detection of finer structures. Nevertheless, A_V(*Planck*) can effectively trace highly dense regions, with A_V values reaching up to around 90 mag, due to its reliance on far-infrared (FIR) dust emission, which can be observed even in regions where starlight is significantly obscured. When comparing A_V(XPNICER), i.e. $A_V^{90}(X_0 = 80)$, to A_V(Green2019), one obvious difference was that A_V(XPNICER) revealed more small-scale structures due to its higher resolution. Moreover, the dense regions in A_V(XPNICER) often correspond to unreasonably low-extinction features in A_V(Green2019). This discrepancy arises from the limitations of optical surveys, which become star-limited in areas of high column density. Consequently, compared to extinction maps derived from optical surveys such as A_V(Green2019), A_V(XPNICER) is better suited for tracing relatively dense dust structures.

5.2 Detailed comparison with extinction map derived by M. Zhang & J. Kainulainen (2022)

Fig. 6 presents a pixel-by-pixel comparison between A_V(XPNICER) and A_V(Zhang2022) for the region shown in Fig. 5. Fig. 6(a) displays the comparison using all pixels from the A_V(XPNICER) map, while Fig. 6(b) includes only the reliable pixels, defined as those with a background source number density greater than 10. We can see that A_V(XPNICER) agrees well with A_V(Zhang2022) within the low extinction range of approximately 5–15 mag. However, beyond ∼15–20 mag, notable discrepancies arise, with A_V(XPNICER) appearing to overestimate extinction values compared to A_V(Zhang2022) in regions with high extinction.

The systematic differences between A_V(XPNICER) and A_V(Zhang2022) could result from the use of different stellar reference catalogues, each introducing its own zero-point offset into the corresponding XPNICER extinction maps. In our study, we used the *Gaia* DR3 GSP-Phot extinction measurements (R. Andrae et al. 2023) as the reference, whereas A_V(Zhang2022) was based on stellar extinctions from the StarHorse2019 catalogue (F. Anders et al. 2019). As reported by R. Andrae et al. (2023), there is a known systematic offset between these catalogues: extinctions from StarHorse catalogues are typically higher than those from *Gaia* DR3 GSP-Phot, especially in regions with high extinction. To reduce the impact of these zero-point offsets, we applied separate zero-point corrections to each map using a third reference catalogue from X. Zhang et al. (2023) (see Section 4.1). Ideally, this calibration should remove systematic biases and bring the corrected maps into agreement across all levels of extinction. In practice, however, this correction is limited by the depth of the X. Zhang et al. (2023)'s catalogue, which primarily includes stars with extinction values up to approximately $A_V \sim 10$ mag. As a result, the corrections in regions with higher extinction are subject to significant uncertainties due to the lack of suitable calibration stars. These limitations lead to residual systematic differences between the two maps in areas of high extinction.

Overall, while A_V(XPNICER) shows agreement with A_V(Zhang2022) in low-extinction areas, it overestimates extinction values in high-extinction regions due to significant differences between the reference sources used in this study and those in M. Zhang & J. Kainulainen (2022).

Downloaded from https://academic.oup.com/mnras/article/543/4/3830/8276728 by guest on 30 October 2025

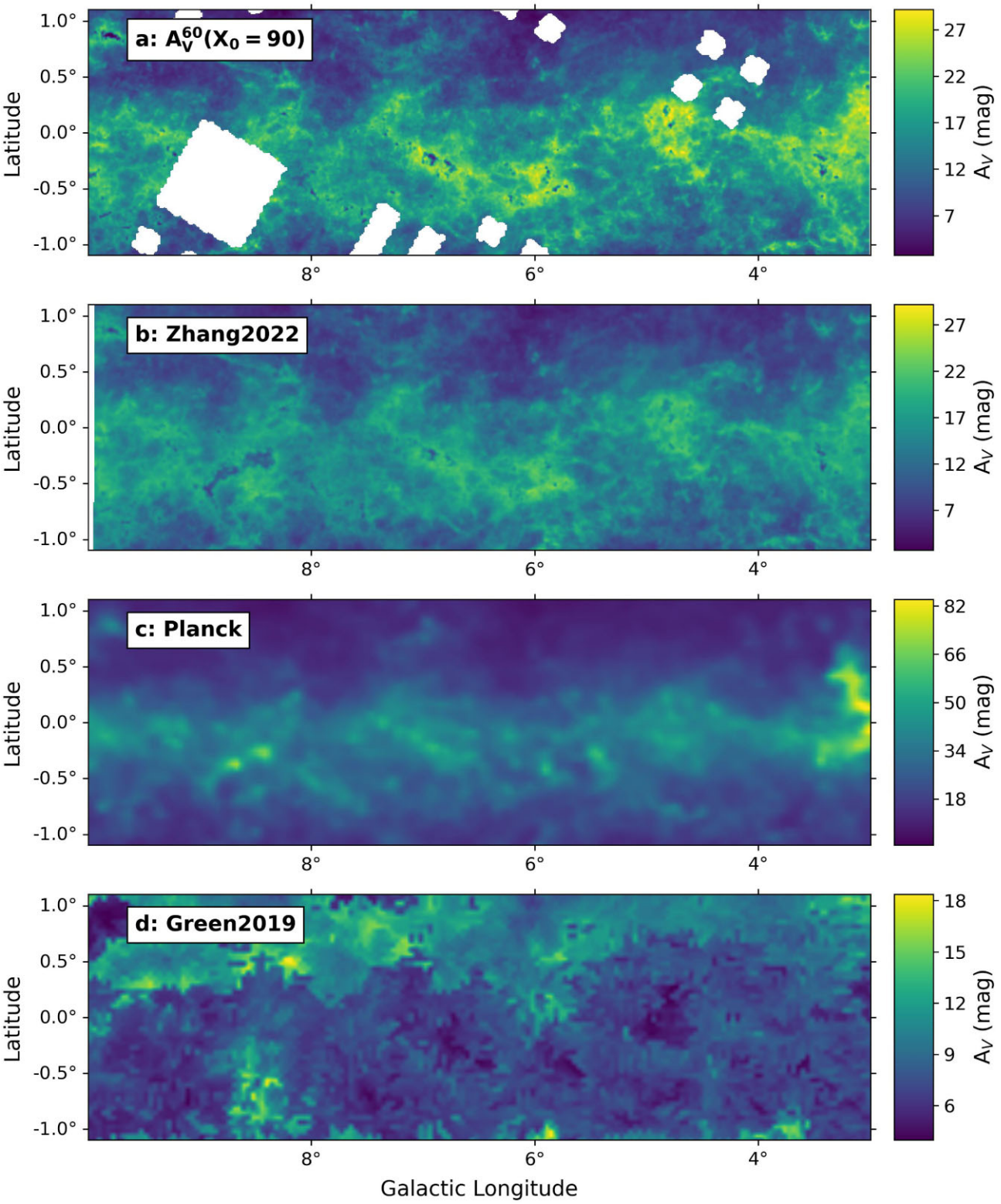

Figure 5. Zoom-in view of a section in the inner Galactic plane of (a) our $A_V^{60}(X_0 = 90)$ map; (b) XPNICER extinction map obtained by M. Zhang & J. Kainulainen (2022). We also corrected the zero-point offset of this map using the method described in Section 4.1; (c) *Planck* dust map (Planck Collaboration XI 2014); and (d) integrated 3D extinction map obtained by G. M. Green et al. (2019).

Downloaded from https://academic.oup.com/mnras/article/543/4/3830/8276728 by guest on 30 October 2025

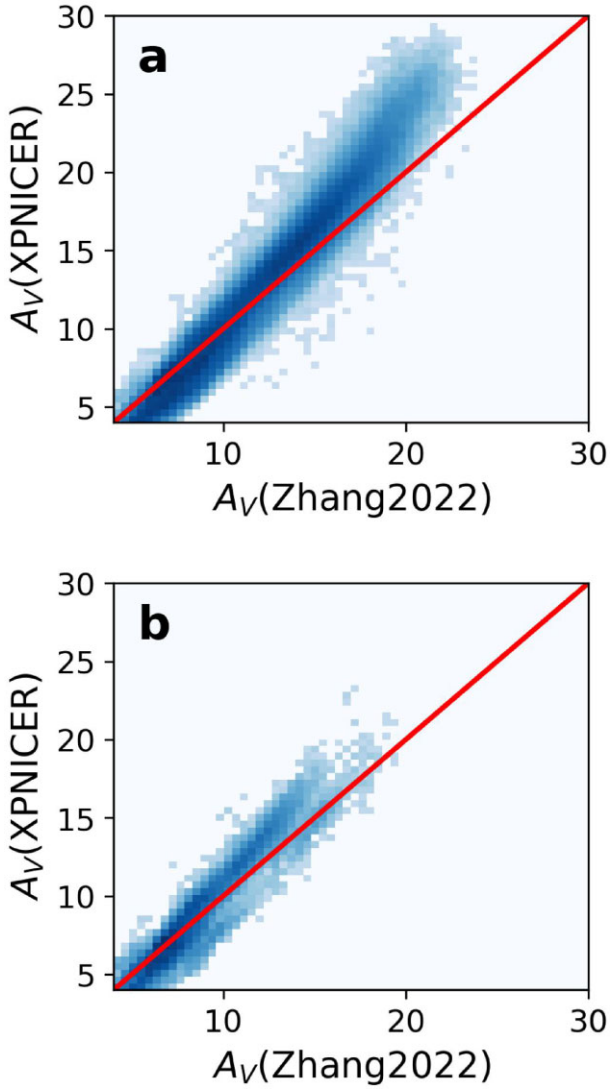

Figure 6. Pixel-by-pixel comparison between our extinction map A_V(XPNICER) and the previous XPNICER extinction map A_V(Zhang2022) from M. Zhang & J. Kainulainen (2022) for (a) all pixels and (b) reliable pixels with background source number density of >10. The solid lines represent the one-to-one correspondence. We have corrected the zero-point offset of A_V(Zhang2022) using the method described in Section 4.1.

5.3 Detailed comparison with *Planck* dust map

Planck Collaboration XI (2014) developed an all-sky dust model that utilized emission data from both the *Planck* and *IRAS* (*Infrared Astronomical Satellite*) surveys. This model fits the SED of the emission using a modified blackbody, assuming thermal equilibrium in the optically thin regime. The resulting all-sky map of τ_{353} was produced at a resolution of 5 arcmin.

We retrieved the $\tau_{353}(Planck)$ using the PYTHON interface provided by DUSTMAPS (G. M. Green 2018). For consistency, we also converted A_V(XPNICER) back to A_K units, denoted as A_K(XPNICER), following the reddening law proposed by S. Wang & X. Chen (2019). Fig. 7 displays the pixel-to-pixel comparison between A_K(XPNICER) and $\tau_{353}(Planck)$ across the entire A_K(XPNICER) map. There is an approximate linear relationship for $\tau_{353}(Planck) \lesssim 5 \times 10^{-4}$, but significant discrepancies appear when $\tau_{353}(Planck) \gtrsim 5 \times 10^{-4}$. These discrepancies in dense regions could result from

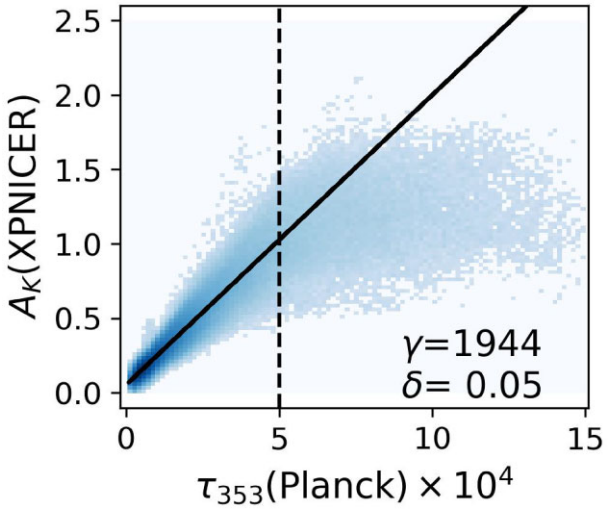

Figure 7. Pixel-to-pixel comparison between our XPNICER extinction map and the *Planck* dust map (Planck Collaboration XI 2014). The black solid line represents the linear fit with a slope of γ and an intercept of δ. The fitting was constrained to $\tau_{353} < \tau_{\rm cut} \times 10^{-4}$, where $\tau_{\rm cut} = 5$, as indicated by the vertical black dashed line. The fitting parameters are also displayed in the figure.

biases in A_K(XPNICER) due to limitations in our extinction mapping technique, as noted by M. Zhang & J. Kainulainen (2022).

We also applied a linear fit to the relationship between A_K(XPNICER) and $\tau_{353}(Planck)$, described by the following equation:

$$A_K(\mathrm{XPNICER}) = \gamma \tau_{353}(Planck) + \delta. \quad (4)$$

The fitting was constrained to the range where $\tau_{353}(Planck) < \tau_{\rm cut} \times 10^{-4}$, with $\tau_{\rm cut}$ set to 5. The resulting values for the fitting parameters were $\gamma = 1944$ and $\delta = 0.05$. Similarly, M. Zhang & J. Kainulainen (2022) performed a comparison between their XPNICER extinction map and the *Planck* dust map (Planck Collaboration XI 2014) using the same linear fitting approach. They obtained fitting parameters of $\gamma_{\rm Zhang2022} = 2043$ and $\delta_{\rm Zhang2022} = 0.3$.

The intercept value of $\delta = 0.05$ from our fit suggests that A_K(XPNICER) might systematically overestimate A_K values by about 0.05 in low-extinction regions, which corresponds to an A_V value of approximately 0.6 mag. This systematic offset could be attributed to the zero-point uncertainty in our extinction map (see Section 4.1) and the uncertainty in the *Planck* dust maps.

The slope of the linear fit, represented by γ, is proportional to the ratio of dust opacity to extinction coefficient, as indicated by M. Lombardi et al. (2014), and is related to dust properties such as composition and grain size distribution (V. Ossenkopf & T. Henning 1994). M. Zhang & J. Kainulainen (2022) found that their $\gamma_{\rm Zhang2022} = 2043$ was reasonably within the range of approximately 1000–6000, as inferred by previous studies (C. Kramer et al. 2003; M. Lombardi et al. 2014; E. Zari et al. 2016; S. Meingast et al. 2018). Our similar value of $\gamma = 1944$ should also be consistent with the findings of those prior studies.

5.4 Detailed comparison with 3D extinction map by G. M. Green et al. (2019)

We accessed the 3D extinction map presented by G. M. Green et al. (2019) using the DUSTMAPS PYTHON interface (G. M. Green 2018)

Downloaded from https://academic.oup.com/mnras/article/543/4/3830/8276728 by guest on 30 October 2025

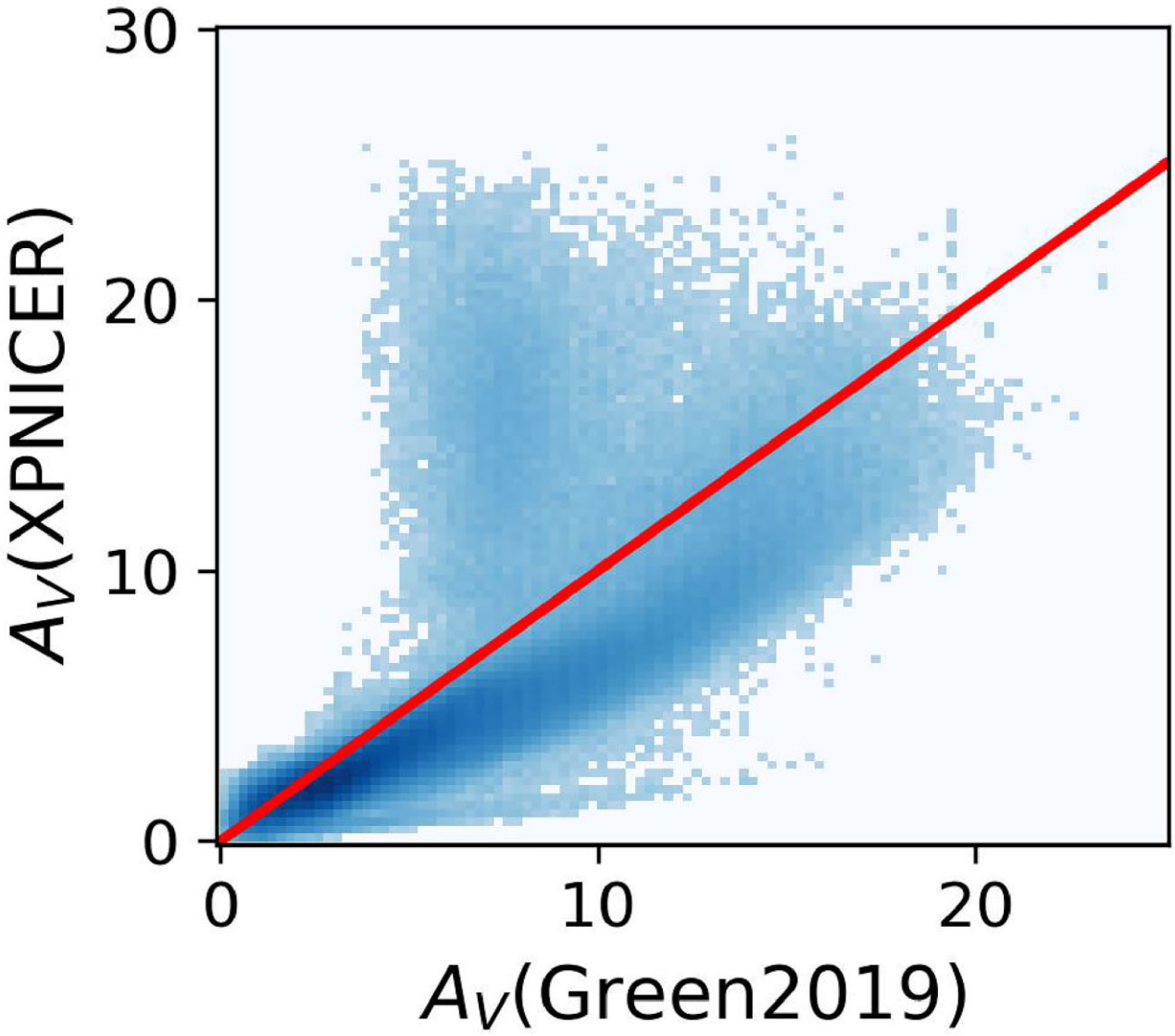

Figure 8. Pixel-to-pixel comparison between our XPNICER extinction map and the integrated 3D extinction map by G. M. Green et al. (2019). The solid line represents the one-to-one relation.

and integrated it up to a distance of 63 kpc to generate a projected extinction map. This process ultimately provided the integrated 2D extinction map of A_V(Green2019).

Fig. 8 displays the pixel-to-pixel comparison between A_V(XPNICER) and A_V(Green2019). While a general correlation is observed between the two maps, A_V(XPNICER) also shows a rough agreement with A_V(Green2019) in low-extinction regions. However, in high-extinction regions (A_V(Green2019) $\gtrsim$ 5 mag), A_V(XPNICER) values are noticeably higher than those in A_V(Green2019). This discrepancy likely arises from the limitations of optical surveys, where there are insufficient optical stars to accurately estimate extinction in higher extinction regions, as seen in extinction maps based on optical surveys like G. M. Green et al. (2019).

6 SUMMARY AND CONCLUSIONS

We have generated 2D dust extinction maps with spatial resolutions ranging from 30 to 300 arcsec using the UKIDSS/GPS photometric catalogue (P. W. Lucas et al. 2008). These maps cover the entire ∼1800 deg^2 area of the Galactic plane surveyed by UKIDSS/GPS. The maps were produced utilizing the XPNICER technique (M. Zhang & J. Kainulainen 2022), an advancement of the previous PNICER (S. Meingast et al. 2017) and Xpercentile (K. Dobashi et al. 2008) methods. The primary findings and conclusions are summarized as follows:

(i) We developed a set of novel dust extinction maps covering the UKIDSS/GPS survey area, employing the XPNICER mapping technique. These maps, with spatial resolutions of 30–300 arcsec, are capable of tracing dust extinction up to $A_V \sim 35$ mag. They reflect the total extinction up to distances ranging from ∼2 to 20 kpc, which vary significantly depending on the line of sight. We have also made these extinction maps, along with the associated uncertainty and number density maps, available at https://doi.org/10.57760/sciencedb.12869.

(ii) The typical uncertainty in our XPNICER A_V map is approximately 0.2 mag. As suggested by M. Zhang & J. Kainulainen

Downloaded from https://academic.oup.com/mnras/article/543/4/3830/8276728 by guest on 30 October 2025

(2022), sources of this uncertainty include observed photometric errors, variations in intrinsic colours, and biases in reference stars. Additionally, the zero-point offset of our XPNICER map is from 0.2 to 4.5 mag, varying towards the different lines of sight. The systematic uncertainties arising from different extinction laws and other unclear origins can even reach $\gtrsim$20–30 per cent.

(iii) Compared to several previous dust-based maps, our XPNICER maps offer higher spatial resolution and better trace regions with relatively high dust extinction than extinction maps based on optical surveys like *Gaia*. It serves as a high-fidelity extinction-based map, providing a complementary and independent measure of dust column densities.

Despite representing a significant advancement, our extinction map still struggles to accurately trace extremely dense dust structures due to the limited sensitivity of current surveys. In future, upcoming optical or infrared imaging surveys such as LSST (Large Synoptic Survey Telescope) or *JWST* (*James Webb Space Telescope*) will offer unprecedented deep photometry, which can be used to create more refined extinction maps using our XPNICER technique. This work is part of the PROMISE[5] program, which aims to derive high-dynamic-range column density data for molecular clouds by combining MIR extinction, FIR dust emission, and NIR extinction data.

ACKNOWLEDGEMENTS

We acknowledge the support from the National Key Research and Development Program of China with grant 2023YFA1608000. This work was supported by the National Natural Science Foundation of China (grant nos 12473026, 12303033, and 12073079). This project has received funding from the European Union's Horizon 2020 Framework Programme under grant agreement no. 639459 (PROMISE). This research has made use of ASTROPY,[6] a community-developed core PYTHON package for astronomy (Astropy Collaboration 2013, 2018). This research has made use of the VizieR catalogue access tool, CDS, Strasbourg, France (DOI: 10.26093/cds/vizier). The original description of the VizieR service was published in 2000, A&AS, 143, 23.

DATA AVAILABILITY

We have made available the extinction maps, along with corresponding uncertainty and number density maps, produced using the XPNICER technique based on the UKIDSS/GPS photometric catalogues at https://doi.org/10.57760/sciencedb.12869. These maps are provided in a multi-extension FITS file format, with detailed explanations included in the file header.

REFERENCES

Alonso-García J. et al., 2017, ApJ, 849, L13
Alves J., Lombardi M., Lada C. J., 2014, A&A, 565, A18
Anders F. et al., 2019, A&A, 628, A94
Andrae R. et al., 2018, A&A, 616, A8
Andrae R. et al., 2023, A&A, 674, A27
Astropy Collaboration, 2013, A&A, 558, A33
Astropy Collaboration, 2018, AJ, 156, 123
Babusiaux C. et al., 2023, A&A, 674, A32
Bai Y., Liu J., Wang Y., Wang S., 2020, AJ, 159, 84
Butler R. E., Salim S., 2024, ApJ, 963, 59
Cardelli J. A., Clayton G. C., Mathis J. S., 1989, ApJ, 345, 245
Casali M. et al., 2007, A&A, 467, 777
Chambers K. C. et al., 2016, preprint (arXiv:1612.05560)
Chen B. Q. et al., 2019, MNRAS, 483, 4277
Creevey O. L. et al., 2023, A&A, 674, A26
Dharmawardena T. E., Bailer-Jones C. A. L., Fouesneau M., Foreman-Mackey D., Coronica P., Colnaghi T., Müller T., Wilson A. G., 2024, MNRAS, 532, 3480
Dobashi K., 2011, PASJ, 63, S1
Dobashi K., Bernard J. P., Hughes A., Paradis D., Reach W. T., Kawamura A., 2008, A&A, 484, 205
Draine B. T., 2009, in Henning T., Grün E., Steinacker J., eds, ASP Conf. Ser. Vol. 414, Cosmic Dust – Near and Far. Astron. Soc. Pac., San Francisco, p. 453
Drew J. E. et al., 2005, MNRAS, 362, 753
Edenhofer G., Zucker C., Frank P., Saydjari A. K., Speagle J. S., Finkbeiner D., Enßlin T. A., 2024, A&A, 685, A82
Flewelling H. A. et al., 2020, ApJS, 251, 7
Fouesneau M. et al., 2023, A&A, 674, A28
Gaia Collaboration, 2016, A&A, 595, A1
Gaia Collaboration, 2023, A&A, 674, A1
Gao Y., Solomon P. M., 2004, ApJ, 606, 271
Girardi L., Groenewegen M. A. T., Hatziminaoglou E., da Costa L., 2005, A&A, 436, 895
Goodman A. A., Pineda J. E., Schnee S. L., 2009, ApJ, 692, 91
Green G. M., 2018, J. Open Source Softw., 3, 695
Green G. M., Schlafly E., Zucker C., Speagle J. S., Finkbeiner D., 2019, ApJ, 887, 93
Greiss S. et al., 2012, AJ, 144, 24
Hambly N. C. et al., 2008, MNRAS, 384, 637
Hewett P. C., Warren S. J., Leggett S. K., Hodgkin S. T., 2006, MNRAS, 367, 454
Hodgkin S. T., Irwin M. J., Hewett P. C., Warren S. J., 2009, MNRAS, 394, 675
Hosek M. W. J. et al., 2018, ApJ, 855, 13
Hottier C., Babusiaux C., Arenou F., 2020, A&A, 641, A79
Irwin M. J., 2008, in Kaufer A., Kerber F., eds, The 2007 ESO Instrument Calibration Workshop. Springer-Verlag, Berlin, p. 541
Juvela M., Montillaud J., 2016, A&A, 585, A38
Kainulainen J., Lehtinen K., Harju J., 2006, A&A, 447, 597
Kainulainen J., Lehtinen K., Väisänen P., Bronfman L., Knude J., 2007, A&A, 463, 1029
Kainulainen J., Beuther H., Henning T., Plume R., 2009, A&A, 508, L35
Kainulainen J., Alves J., Beuther H., Henning T., Schuller F., 2011, A&A, 536, A48
Kramer C., Richer J., Mookerjea B., Alves J., Lada C., 2003, A&A, 399, 1073
Lada C. J., Lada E. A., Clemens D. P., Bally J., 1994, ApJ, 429, 694
Lada C. J., Lombardi M., Alves J. F., 2010, ApJ, 724, 687
Lallement R., Babusiaux C., Vergely J. L., Katz D., Arenou F., Valette B., Hottier C., Capitanio L., 2019, A&A, 625, A135
Lallement R., Vergely J. L., Babusiaux C., Cox N. L. J., 2022, A&A, 661, A147
Lawrence A. et al., 2007, MNRAS, 379, 1599
Leike R. H., Enßlin T. A., 2019, A&A, 631, A32
Leike R. H., Glatzle M., Enßlin T. A., 2020, A&A, 639, A138
Lombardi M., 2005, A&A, 438, 169
Lombardi M., 2009, A&A, 493, 735
Lombardi M., 2018, A&A, 615, A174
Lombardi M., Alves J., 2001, A&A, 377, 1023
Lombardi M., Alves J., Lada C. J., 2006, A&A, 454, 781
Lombardi M., Lada C. J., Alves J., 2008, A&A, 489, 143
Lombardi M., Lada C. J., Alves J., 2010, A&A, 512, A67

[5] http://promise.jounikainulainen.com
[6] http://www.astropy.org

Downloaded from https://academic.oup.com/mnras/article/543/4/3830/8276728 by guest on 30 October 2025

Lombardi M., Bouy H., Alves J., Lada C. J., 2014, A&A, 566, A45
Lucas P. W. et al., 2008, MNRAS, 391, 136
Lynga G., 1982, A&A, 109, 213
Maíz Apellániz J., Pantaleoni González M., Barbá R. H., García-Lario P., Nogueras-Lara F., 2020, MNRAS, 496, 4951
Marsh K. A. et al., 2017, MNRAS, 471, 2730
Marshall D. J., Robin A. C., Reylé C., Schultheis M., Picaud S., 2006, A&A, 453, 635
Meingast S., Lombardi M., Alves J., 2017, A&A, 601, A137
Meingast S., Alves J., Lombardi M., 2018, A&A, 614, A65
Minniti D. et al., 2010, New Astron., 15, 433
Monguió M. et al., 2020, A&A, 638, A18
Ossenkopf V., Henning T., 1994, A&A, 291, 943
Padoan P., Federrath C., Chabrier G., Evans N. J., II, Johnstone D., Jørgensen J. K., McKee C. F., Nordlund Å., 2014, in Beuther H., Klessen R. S., Dullemond C. P., Henning T., eds, Protostars and Planets VI. Univ. Arizona Press, Tucson, AZ, p. 77
Planck Collaboration XI, 2014, A&A, 571, A11
Queiroz A. B. A. et al., 2020, A&A, 638, A76
Queiroz A. B. A. et al., 2023, A&A, 673, A155
Rezaei Kh. S., Bailer-Jones C. A. L., Schlafly E. F., Fouesneau M., 2018, A&A, 616, A44
Rieke G. H., Lebofsky M. J., 1985, ApJ, 288, 618
Robin A. C., Reylé C., Derrière S., Picaud S., 2003, A&A, 409, 523
Rybizki J. et al., 2022, MNRAS, 510, 2597
Sanders J. L., Smith L., González-Fernández C., Lucas P., Minniti D., 2022, MNRAS, 514, 2407
Scaringi S. et al., 2018, MNRAS, 481, 3357
Scaringi S., Monguió M., Knigge C., Fratta M., Gänsicke B., Groot P. J., Rebassa-Mansergas A., Toloza O., 2023, MNRAS, 518, 3137
Schlafly E. F., Finkbeiner D. P., 2011, ApJ, 737, 103
Schlegel D. J., Finkbeiner D. P., Davis M., 1998, ApJ, 500, 525
Schultheis M. et al., 2014, A&A, 566, A120
Skrutskie M. F. et al., 2006, AJ, 131, 1163
Spilker A., Kainulainen J., Orkisz J., 2021, A&A, 653, A63
Vergely J. L., Lallement R., Cox N. L. J., 2022, A&A, 664, A174
Wang S., Chen X., 2019, ApJ, 877, 116
Wang S., Jiang B. W., 2014, ApJ, 788, L12
Wang S., Gao J., Jiang B. W., Li A., Chen Y., 2013, ApJ, 773, 30
Zari E., Lombardi M., Alves J., Lada C. J., Bouy H., 2016, A&A, 587, A106
Zhang M., Kainulainen J., 2019, A&A, 632, A85
Zhang M., Kainulainen J., 2022, MNRAS, 517, 5180
Zhang M., Kainulainen J., Mattern M., Fang M., Henning T., 2019, A&A, 622, A52
Zhang X., Green G. M., Rix H.-W., 2023, MNRAS, 524, 1855
Zhao H., Wang S., Jiang B., Li J., Fan D., Ren Y., Ma X., 2024, ApJ, 974, 138

APPENDIX A: COMPARISON OF SOURCE NUMBER DENSITY BETWEEN UKIDSS/GPS AND PAN-STARRS1 SURVEY

We extracted about 426 million NIR point sources from the UKIDSS/GPS and 2MASS catalogues. Specifically, this includes about 412 million unsaturated point sources from the UKIDSS/GPS catalogue, and around 14 million bright sources from the 2MASS catalogue within the UKIDSS/GPS survey region, selected with magnitude thresholds of $J < 13.25$, $H < 12.75$, or $K < 12.0$ mag. Fig. A1 presents the number density maps of these ∼426 million NIR sources. The source density varies from a few to several hundred sources per arcmin^2, with a median value of approximately 30 arcmin^{-2}.

The Pan-STARRS1 (PS1) telescope, located on Mount Haleakala, Hawaii, is equipped with the Gigapixel Camera #1. From 2010 to 2014, PS1 conducted the multi-epoch 3π survey, covering the northern sky ($\delta > -30^\circ$) in five broad-band filters: $g_{\rm P1}$, $r_{\rm P1}$, $i_{\rm P1}$, $z_{\rm P1}$, and $y_{\rm P1}$. The single-epoch imaging reaches 5σ depths (AB magnitudes) of 22.0, 21.8, 21.5, 20.9, and 19.7 mag in the $g_{\rm P1}$, $r_{\rm P1}$, $i_{\rm P1}$, $z_{\rm P1}$, and $y_{\rm P1}$ bands, respectively (K. C. Chambers et al. 2016). We retrieved mean photometric measurements of point sources from DR2, which were obtained by averaging detections across all epochs. The data were accessed using the *Mikulski Archive for Space Telescopes* Pan-STARRS catalogue API[7] through an SQL query. We selected objects with valid mean magnitudes in at least the $g_{\rm P1}$ and $r_{\rm P1}$ bands. To exclude sources affected by artefacts, we further required QF_PERFECT > 0.85 in both $g_{\rm P1}$ and $r_{\rm P1}$. Finally, point sources were identified by requiring a small difference (<0.05 mag) between the Kron and PSF magnitudes in the $r_{\rm P1}$ band, following the criteria of H. A. Flewelling et al. (2020).

We ultimately obtained approximately 153 million point sources from the PS1 survey within the UKIDSS/GPS survey region. Fig. A1 presents the number density maps of PS1 point sources. As evident from the comparison, the source number density in PS1 is significantly lower than that of UKIDSS/GPS, particularly in regions with high column density. The median number density of PS1 sources

[7]https://catalogs.mast.stsci.edu/docs/panstarrs.html

Downloaded from https://academic.oup.com/mnras/article/543/4/3830/8276728 by guest on 30 October 2025

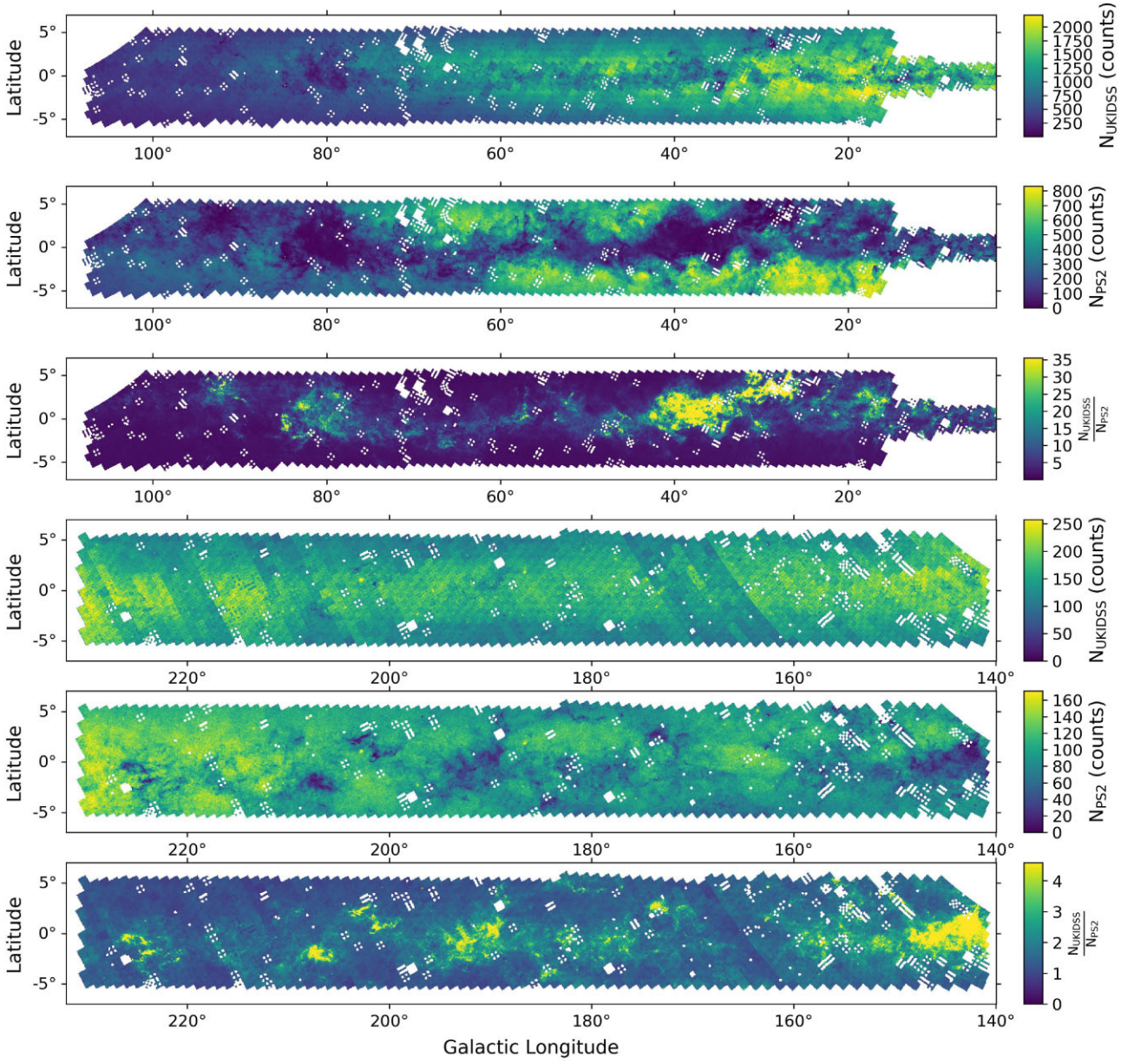

Figure A1. Point source number density maps from UKIDSS/GPS and Pan-STARRS, and their ratio map, shown over the UKIDSS/GPS survey region at a spatial resolution of 180 arcsec.

is about 13 arcmin^{-2}. To quantify this difference, we calculated the ratio of UKIDSS/GPS source number density ($N_{\rm UKIDSS}$) to PS1 source number density ($N_{\rm PS1}$), as shown in Fig. A1. In some dense regions, the ratio exceeds 40, with a median value of ∼2 across the survey area.

APPENDIX B: COMPARISON OF DIFFERENT CROSS-MATCHING RESULTS WITH AND WITHOUT CONSIDERING PROPER MOTIONS

In Section 2.3, we cross-matched about 426 million UKIDSS/GPS sources with around 52 million *Gaia* DR3 sources, without applying proper motion corrections, resulting in a matched sample of about 50 million sources. The UKIDSS/GPS observations were conducted between 2005 and 2013, while the *Gaia* mission began its science operations in 2014. Given this time gap, a precise cross-match would ideally account for source proper motions and the reference epochs of both surveys.

Gaia DR3 provides proper motion measurements for all sources. Ideally, the *Gaia* astrometry should be propagated individually to the epoch of each UKIDSS/GPS observation before performing the cross-match. However, the UKIDSS/GPS catalogue is a merged data set constructed from single-band detections taken at different epochs. Therefore, a proper propagation of *Gaia* astrometry would require tracing back to the single-band detection tables, applying proper motion corrections to their positions, and then performing the band-merging step based on these corrected positions, following the procedure described in the UKIDSS pipeline (N. C. Hambly et al. 2008; M. J. Irwin 2008). Such a detailed treatment is beyond the scope of this paper.

Downloaded from https://academic.oup.com/mnras/article/543/4/3830/8276728 by guest on 30 October 2025

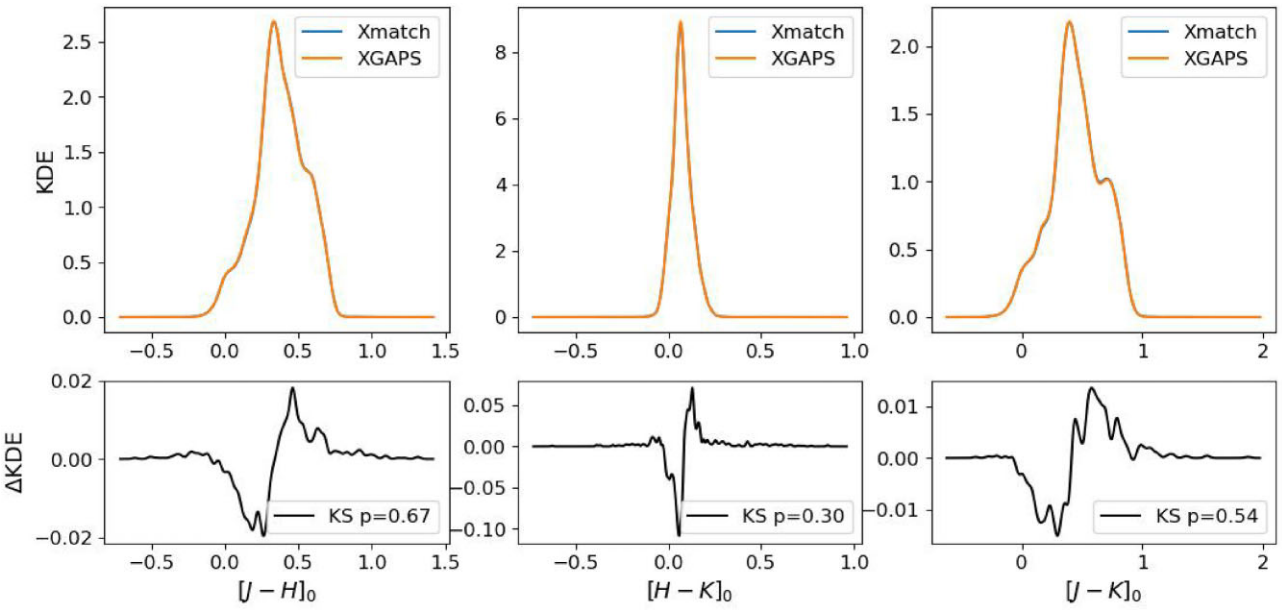

Figure B1. KDEs (top) and KDE difference (bottom) of the intrinsic colours of $J-H$ (left), $H-K$ (middle), and $J-K$ (right) from Xmatch and XGAPS cross-matched sources, respectively.

S. Scaringi et al. (2018) developed a sub-arcsecond cross-matching method and applied it to create a matched catalogue between *Gaia* DR2, the INT Photometric H α Survey (IPHAS) DR2 of the northern Galactic plane (J. E. Drew et al. 2005), and the *Kepler*-INT Survey (KIS; S. Greiss et al. 2012). To avoid recalculating the *Gaia* astrometry for every individual source, they divided the IPHAS and KIS catalogues into monthly epoch batches. For each batch, they assumed that the observations in different bands for a given source occurred within a short time interval, allowing them to adopt the start of the single-band observations as a reference epoch. They then propagated the *Gaia* positions and proper motions to the mid-point epoch of each month. Following this approach, S. Scaringi et al. (2023) applied the same technique to cross-match *Gaia* DR3 with the INT Galactic Plane Surveys (IGAPS; M. Monguió et al. 2020) and UKIDSS/GPS. The resulting catalogue, called XGAPS, contains about 33 million *Gaia* DR3 sources with IGAPS photometry, of which approximately 20 million also have UKIDSS/GPS measurements.

We downloaded the XGAPS catalogue from ViZieR,[8] which provides precise cross-matches between *Gaia* DR3 and UKIDSS/GPS sources for about 33 million *Gaia* DR3 objects. Independently, we performed a direct cross-match of these same *Gaia* DR3 sources with the UKIDSS/GPS catalogue using a matching tolerance of 0.5 arcsec as described in Section 2.3 (hereafter referred to as Xmatch). While Xmatch does not account for proper motions, XGAPS includes proper motion corrections to improve matching accuracy. We then compared the results from these two cross-matching methods.

We randomly selected 100 000 sources from the ∼33 million *Gaia* DR3 objects, among which about 76 000 have counterparts in the UKIDSS/GPS catalogue based on our Xmatch cross-match. Of these ∼76 000 sources, roughly 72 000 also have counterparts in the UKIDSS/GPS catalogue according to the XGAPS cross-match. This implies that about 5 per cent of matches are mismatches when proper motions are not taken into account in the cross-matching process. Since the Xmatch catalogue is used to statistically estimate the intrinsic colours of UKIDSS/GPS sources, the presence of these mismatches should not significantly impact extinction estimates if the intrinsic colour distributions from Xmatch and XGAPS samples are statistically similar. Fig. B1 presents the kernel density estimations (KDEs) of the intrinsic colours $J-H$, $H-K$, and $J-K$ for the ∼76 000 Xmatch-matched sources and the ∼72 000 XGAPS-matched sources. The KDEs show only minor differences between the two samples. Supporting this, two-sample Kolmogorov–Smirnov tests yield p-values greater than 0.05 for all intrinsic colours, indicating that the null hypothesis – that the two samples come from the same distribution – cannot be rejected. Repeating this process 1000 times, we consistently find a mismatch contamination rate of 5–6 per cent when proper motions are ignored during the cross-match between *Gaia* DR3 and UKIDSS/GPS. However, the intrinsic NIR colours of sources matched without proper motion corrections remain statistically indistinguishable from those matched with proper motion considered.

Overall, directly cross-matching *Gaia* DR3 and UKIDSS/GPS without accounting for proper motions results in approximately 5–6 per cent mismatches. However, these mismatches do not significantly affect the statistical distribution of the intrinsic NIR colours of the matched sources. Therefore, from a statistical view, neglecting proper motion corrections in the cross-match does not significantly affect our extinction estimates for UKIDSS/GPS sources.

[8] https://cdsarc.cds.unistra.fr/viz-bin/cat/J/MNRAS/518/3137

APPENDIX C: CLOSE VIEW OF OUR XPNICER EXTINCTION MAP

Downloaded from https://academic.oup.com/mnras/article/543/4/3830/8276728 by guest on 30 October 2025

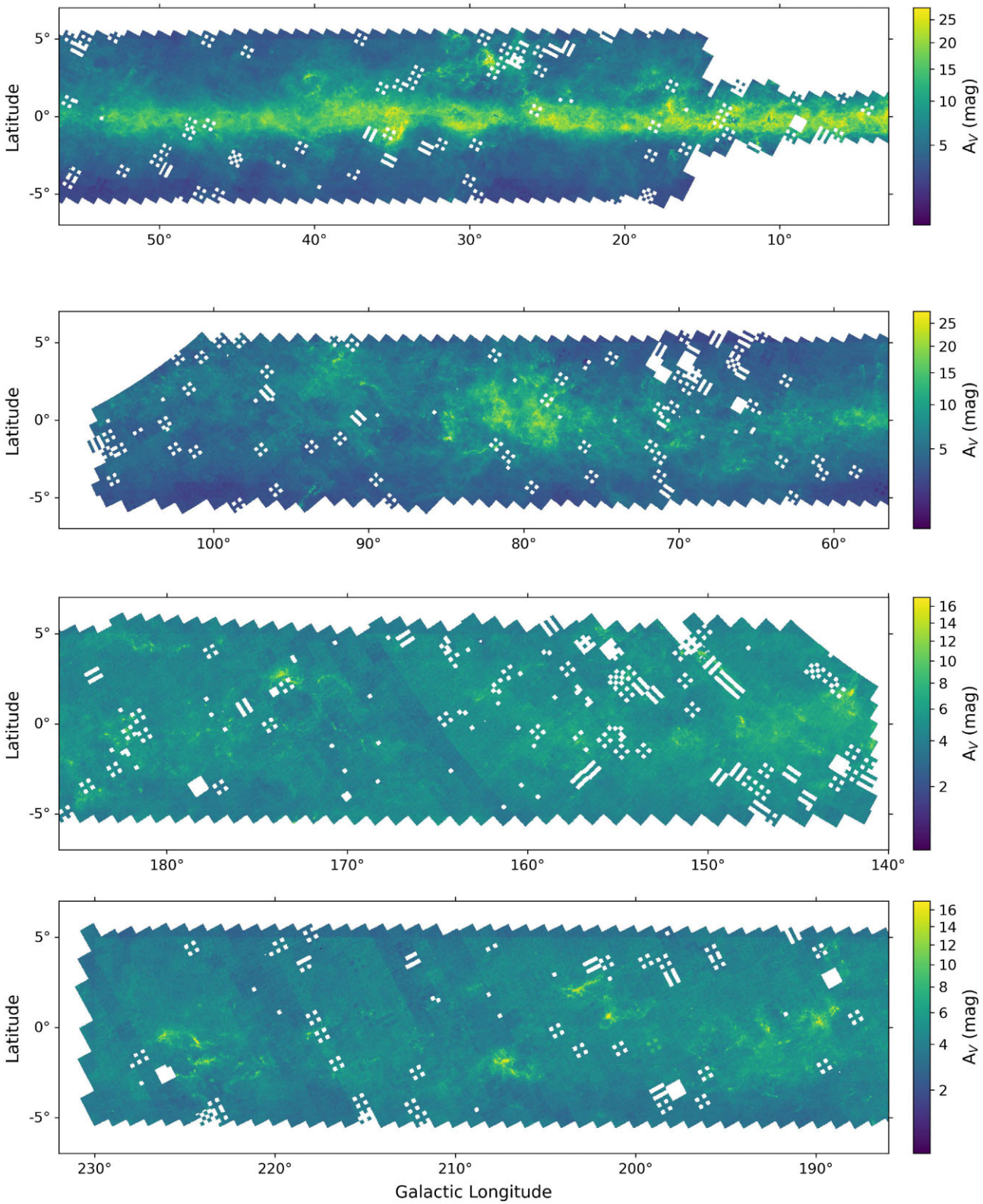

Figure C1. The XPNICER extinction maps of background sources obtained using $X_0 = 80$ per cent and $X_1 = 95$ per cent with the spatial resolution of 90 arcsec for the Galactic plane area covered by UKIDSS/GPS. The zero-point offset has been subtracted from the extinction map.

Downloaded from https://academic.oup.com/mnras/article/543/4/3830/8276728 by guest on 30 October 2025

APPENDIX D: TILE PATTERNS IN THE MAPS

Tile patterns are visible in $A_V^{90}(X_0 = 80)$, $\delta A_V^{90}(X_0 = 80)$, and $N_{\rm bg}^{90}(X_0 = 80)$, as shown in Fig. 2. These patterns are particularly noticeable in the outer Galactic plane, for example, in several curved grid-like structures around $l \sim 160^\circ$–170° and $l \sim 200^\circ$–230°. Fig. D1(a) presents a $10^\circ \times 10^\circ$ section of $A_V^{90}(X_0 = 80)$, where inclined dark tile patterns can be clearly seen.

As noted by M. Zhang & J. Kainulainen (2022), these tile patterns arise from varying sensitivity across the UKIDSS/GPS survey. Due to the different characteristics of detectors and atmospheric conditions, the images observed at different times usually have different sensitivity. This variation occurs on scales corresponding to the field of view or individual detectors, producing the observed tile patterns.

Such patterns can be removed by applying a uniform sensitivity cut, for example a brightness threshold in the K band. Figs D1(b), (c), and (d) show extinction maps generated using background sources with $K < 18$, $K < 17$, and $K < 16$ mag, respectively. While some residual tile patterns remain in panels (b) and (c), the patterns nearly disappear at $K < 16$ mag.

However, this threshold approaches the sensitivity limit of the 2MASS survey, which is much brighter than that of UKIDSS/GPS ($K \sim 18$ mag). Consequently, applying such a magnitude cut reduces the number of background sources, resulting in a significant loss of the resolution and dynamic range of the extinction maps. Therefore, we chose not to correct for tile patterns in this paper.

Downloaded from https://academic.oup.com/mnras/article/543/4/3830/8276728 by guest on 30 October 2025

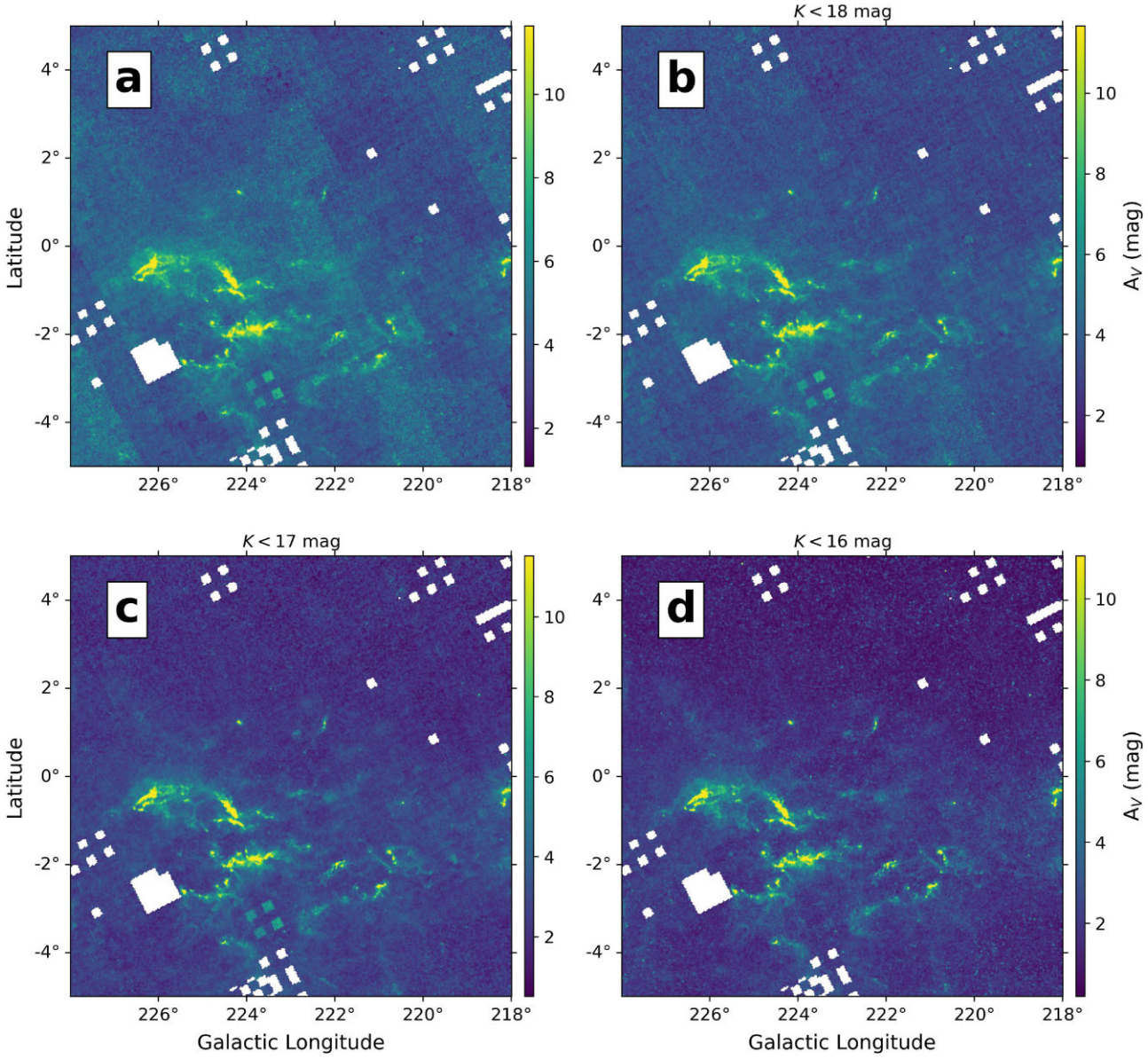

Figure D1. The XPNICER extinction maps ($A_V^{90}(X_0 = 80)$) produced with all background sources (a); background sources with $K < 18$ mag (b); background sources with $K < 17$ mag (c); and background sources with $K < 16$ mag (d) for a $10^\circ \times 10^\circ$ region located at $l = 223^\circ$ and $b = 0^\circ$. The zero-point offset has not been subtracted from these maps.

This paper has been typeset from a TEX/LATEX file prepared by the author.

Downloaded from https://academic.oup.com/mnras/article/543/4/3830/8276728 by guest on 30 October 2025

© The Author(s) 2025.
Published by Oxford University Press on behalf of Royal Astronomical Society. This is an Open Access article distributed under the terms of the Creative Commons Attribution License (https://creativecommons.org/licenses/by/4.0/), which permits unrestricted reuse, distribution, and reproduction in any medium, provided the original work is properly cited.